universität wien

MASTERARBEIT / MASTER'S THESIS

Titel der Masterarbeit / Title of the Master's Thesis

„Characterization of the airborne aerosol inlets used during the A-LIFE field experiment"

verfasst von / submitted by

Manuel Schöberl, BSc

angestrebter akademischer Grad / in partial fulfilment of the requirements for the degree of

Master of Science (MSc)

Wien, 2019 / Vienna 2019

Studienkennzahl lt. Studienblatt / degree programme code as it appears on the student record sheet:	A 066 876
Studienrichtung lt. Studienblatt / degree programme as it appears on the student record sheet:	Masterstudium Physik
Betreut von / Supervisor:	Univ.-Prof. Dr. Bernadett Weinzierl

Contents

Abstract

Understanding mixtures of absorbing aerosol and reducing uncertainties in estimates of radiative forcing of absorbing aerosols is one of the main motivations behind the A-LIFE project. The aircraft measuring campaign to collect data for this project took place in Cyprus in April 2017. An extensive payload of aerosol in-situ instruments was integrated in the DLR research aircraft Falcon to measure different properties of aerosol particles throughout the tropospheric column in the Eastern Mediterranean.

To transport the aerosol particles to the instruments, the isokinetic and sideward aerosol inlets of the Falcon were used. The inlets cause a size-dependent loss of the aerosol particles, potentially leading to significant discrepancies between the observations and the "real" aerosol properties. Therefore, proper interpretation of the data requires careful characterization of the losses at the inlets. Beside the previous mentioned inlets, a characterization of the inlet of an in-cabin instrument detecting cloud condensation nuclei (CCNC), the Cloud Condensation Nuclei Counter (CCNC), is important. This inlet provides a constant pressure for the CCNC measurements. For this purpose, a Constant Pressure System (CPS) was implemented and two different orifices were used to achieve constant pressure in the CCNC.

For the characterization of the isokinetic and the sideward inlet, the cutoff-diameters D_{50} and the corresponding Stokes number Stk_{50} were calculated for different altitudes. The cutoff-diameter D_{50} is an important parameter in aerosol science and designates the particle diameter with 50% sampling efficiency, i.e. 50% of the particles pass the inlet. In this thesis work, the cutoff-diameters were calculated as a function of altitude up to 9.5 km. At an altitude of 500 m the cutoff-diameter of the isokinetic inlet is about 2.4 µm, decreasing to about 1.6 µm at an altitude of 9.5 km. The cutoff-diameter of the sideward inlet at an altitude of 500 m is around 450 nm. At an altitude of 9.5 km, the cutoff-diameter decreases to 200 nm. The calculations for the isokinetic inlet were compared against results from the literature. The characterization of the sideward inlet has been done systematically for the first time.

For the CCNC inlet, a transmission efficiency was derived for both orifices. The transmission efficiency is shown for a particle size range from 300 nm to 1 µm. These results can be used for a correction of the CCN number concentration measured by the CCNC.

Ultimately, this study quantifies uncertainties associated with the aerosol sampling system used during the A-LIFE field experiment. The results of this thesis work will add another level of precision and accuracy to the final data analysis of the project. It is clearly shown in this thesis that particle losses due to the different inlets lead to a distortion of the measurements and appropriate corrections are imperative.

Kurzzusammenfassung

Eine der Hauptmotivationen des A-LIFE Projekts ist, Unsicherheiten in Abschätzungen des Strahlungsantriebs von absorbierenden Aerosolen zu minimieren. Dafür wurden mit einem Messflugzeug in Zypern im April 2017 Daten gesammelt. Um über dem Mittelmeer verschiedenste Eigenschaften des Aerosols zu messen, wurden viele In-situ Messinstrumente in das DLR-Forschungsflugzeug Falcon eingebaut.

Um das Aerosol zu den Instrumenten zu transportieren, wurden der isokinetische und der seitwärtige Einlass des Forschungsflugzeugs Falcon verwendet. Die Einlässe verursachen einen größenabhängigen Verlust an Aerosolpartikeln. Dieser Verlust kann eventuell zu Abweichungen zwischen den gemessenen Eigenschaften und den „wirklichen“ Eigenschaften des Aerosols führen. Für eine korrekte Interpretation der gesammelten Daten ist eine Charakterisierung dieser Einlässe und ihrer Partikelverluste wichtig. Neben den zuvor erwähnten Einlässen wurde außerdem der Einlass eines Messinstruments, das sich in der Kabine des Flugzeugs befindet, charakterisiert. Der Cloud Condensation Nuclei Counter, kurz CCNC, detektiert Wolkenkondensationskerne in der Atmosphäre. Damit die Messung erfolgen kann, wird ein konstanter Druck im Messinstrument benötigt. Um diesen zu gewährleisten, wurden zwei verschiedene kritische Düsen in den Aerosolfluss eingebaut.

Für die Charakterisierung des isokinetischen und des seitwärtigen Einlasses wurden der Cutoff-Durchmesser D_{50} und die dazugehörige Stokeszahl Stk_{50} bei verschiedenen Flughöhen berechnet. Der Cutoff-Durchmesser D_{50} ist ein wichtiger Parameter in der Wissenschaft der Aerosolphysik und bezeichnet den Partikeldurchmesser, bei dem die Zähleffizienz 50% beträgt, das heißt 50% der Partikel mit dieser Größe werden mit dem Aerosoleinlass erfasst. Die Cutoff-Durchmesser wurden als Funktion der Flughöhe bis 9,5 km berechnet. Auf einer Höhe von 500 m beträgt der Cutoff-Durchmesser des isokinetischen Einlasses um die 2,4 µm und sinkt auf 1,6 µm bei 9,5 km Flughöhe. Der Cutoff-Durchmesser des Seitwärtseinlass beträgt auf 500 m Flughöhe 450 nm und nimmt auf 9,5 km auf bis zu 200 nm ab. Die Berechnungen für den isokinetischen Einlass wurden mit Ergebnissen aus der Literatur verglichen. Die Charakterisierung des seitlichen Einlasses wurde erstmals systematisch durchgeführt.

Für den Einlass des CCNC gibt diese Arbeit die größenabhängige Transmissionseffizienz der beiden kritischen Düsen. Die Transmissionseffizienz ist für einen Größenbereich von

300 nm bis 1 µm dargestellt. Diese Resultate können zur Korrektur der gemessenen Konzentrationen des CCNC verwendet werden.

Letztendlich quantifiziert diese Arbeit Unsicherheiten im Zusammenhang mit dem Aerosolmesssystem des Forschungsflugzeugs während des A-LIFE Projekts. Die Resultate der Charakterisierungen tragen maßgeblich dazu bei, dass eine höhere Genauigkeit in der finalen Phase der Datenanalyse des Projekts erzielt werden kann. In dieser Arbeit wird gezeigt, dass die Partikelverluste der verschiedenen Einlässe zu einer verzerrten Aerosolmessung führen und eine Korrektur dieser notwendig ist.

Chapter 1

Introduction

Aerosols are liquid or solid particles suspended in a carrier gas. The suspending gas interacts directly with the particles and has a great effect on their behaviour (Hinds, 1999). Aerosols can influence the earth's climate, e.g. by their interaction with clouds (Boucher et al., 2013). For a better understanding of the effects aerosols can cause on the climate, measurements of their microphysical and optical properties are required. The properties of aerosol particles can be detected by different measuring methods and instruments. The advent of modern instrumentation helped to realize aircraft field campaigns (Wendisch and Brenguier, 2013). Aircraft field campaigns enables to measure the, mostly unaffected, aerosol particles directly in atmosphere and allows for a better investigation of their properties. It is necessary that the measured aerosol sample reflects the same properties as the ambient aerosol. To transport the aerosol particles to the instruments, different inlets and sampling lines are required. The inlets and sampling lines cause a size-dependent loss of the aerosol particles because of gravitational sedimentation, turbulent deposition, inertial deposition from bends and constrictions, and diffusion (Huebert et al. 1990; Hermann et al. 2000; Kulkarni et al., 2011) These effects could potentially lead to significant discrepancies between the observations and the (true) properties of the ambient aerosol. Therefore, a proper interpretation of the data requires careful characterization of the particle loss at inlets and in sampling lines.

This thesis work has been realized at the Aerosol Physics and Environmental Physics group of the University of Vienna under the supervision of Univ.-Prof. Dr. Bernadett Weinzierl, as part of the aircraft measurement campaign A-LIFE. A-LIFE is the abbreviation for "Absorbing aerosol layers in a changing climate: Aging, lifetime and dynamics". It is an European Research Council (ERC) project and one of the main motivations behind the project is to reduce uncertainties in estimates of radiative forcing of absorbing aerosols[1]. The measuring campaign was based in Cyprus in April 2017. An extensive payload of aerosol in-situ instruments was integrated in the Deutsches Zentrum für Luft- und Raumfahrt (DLR) research aircraft Falcon and most of the instruments were located inside the aircraft cabin. A lot of different properties of aerosol particles, like size distribution, mixing state, absorption and the concentration of black carbon, throughout the tropospheric column in the eastern Mediterranean were investigated. Many in-situ

[1] A-LIFE (2017). Available at: www.a-life.at (Accessed: 1 February 2019)

instruments were located inside the aircraft cabin receiving the aerosol sample from inlets of the Falcon.

The aim of this master thesis is to characterize the inlets of the Falcon aircraft, which were used during the A-LIFE field experiment. The thesis focuses on three inlets: the isokinetic inlet, the sideward inlet and the in-cabin inlet of an instrument detecting cloud condensation nuclei, the so-called Cloud Condensation Nuclei Counter (CCNC). The CCNC was located inside the aircraft cabin and its inlet has the function to help establish constant pressure for the measurement. Therefore, two orifices were implemented in the aerosol flow (Dollner, 2015; Walser, 2017). One with a small aperture diameter for a higher pressure drop and one with a larger aperture diameter for a lower pressure drop. The characterization of these inlets was made to investigate the following questions of this thesis:

- What is the size-dependent transmission efficiency of the different inlets?
- How does the inlet transmission efficiency change with aircraft altitude?
- How does the transmission efficiency function of the two orifices used for the CCNC measurements look like?

Therefore, size distributions measured during the A-LIFE field project were compared. For the isokinetic inlet, the number size distribution of the Optical Particle Counter (OPC), receiving its aerosol sample from this inlet, was compared against the number size distribution of the loss-unaffected wing mounted open path Cloud and Aerosol Spectrometer (CAS). The sideward inlet characterization resulted from a comparison of the measured number size distribution of two identical OPCs, one receiving its aerosol sample from the isokinetic inlet and one from the sideward inlet. For the orifices at the CCNC inlet, a comparison was made between the measurements of two identical OPCs again. One OPC was connected to the isokinetic inlet and the other OPC collected the aerosol sample after it passed the orifices.

The results for the isokinetic inlet are compared against findings of Fiebig (2001), who performed a similar characterization for an earlier field campaign. The characterization of the sideward inlet has been done systematically for the first time. For the CCNC inlet, the experimental results of the transmission efficiency from the A-LIFE flights are compared against laboratory data from Dollner (2015) and recalculations from Walser (2017).

This thesis is structured in four chapters. The first chapter covers the theoretical principles for a better understanding of the methods and results of this thesis work. It treats the topics aerosol mechanics, sampling and size distribution. The second chapter covers the methods used to achieve the outcome of this thesis. Details of the A-LIFE field campaign and the airborne measurement setup as well as a description of the OPC and the CAS are included. The chapter closes with the explanation of the used number size distribution retrieval. Chapter 3 represents the results of the characterization of the three inlets used during the A-LIFE field campaign. The results are compared against similar calculations and data from the literature. Furthermore, in the last chapters the characterization is discussed and a conclusion is given.

Chapter 2

Theory

This chapter covers the theoretical principles behind the methods and calculations used in this thesis. The section about aerosol in general and the mechanics of aerosol particles follows the book of Hinds (1999). The following section considering the sampling of aerosol particles is a summary from the books of Hinds (1999) and Kulkarni et al. (2011). The chapter closes with an overview of aerosol particle size distributions based on the books of Hinds (1999), Kulkarni et al. (2011) and Seinfeld and Pandis (2006). Specific references are quoted in the respective sections.

2.1 Aerosol

2.1.1 Introduction

The science of aerosol physics deals with the behaviour of solid or liquid particles suspended in gas. There are different ways and approaches to classify an aerosol. A central parameter is the size of the aerosol particle, because all properties of the aerosol are dependent on it. The size of an aerosol particle is expressed in the form of its diameter D_p. The diameters of aerosol particles cover a wide range from a few nanometers up to several hundred micrometers, which is why a range of different measuring instruments is needed to detect the full range of an aerosol size distribution. Aerosol particles can be spherical, but in most cases they are aspherical. For a better comparison, the size of an aerosol particle is described by an equivalent diameter. The equivalent diameter is the diameter of a spherical particle with the same property of an aspherical particle with respect to a certain physical process. This value can vary due to the method which was used to detect the equivalent diameter. When a particle gets measured by its light scattering, the optical equivalent diameter is measured. Thus it’s the diameter of a spherical particle with the same optical properties than of the observed particle. Concerning an electrical induced motion of the particle, the electrical equivalent diameter is measured. Other methods are inertia and gravity (aerodynamic equivalent diameter) and Brownian motion (diffusion equivalent diameter).

Another important aerosol property is the number concentration, e.g. number of particles per unit volume. The chemical composition of the aerosol is also important and of interest, as well as its origin. The origin of an aerosol is mostly split in natural or anthropogenic.

A further distinction could be the source region, e.g. continental, urban or marine. In addition, a classification is made by the mechanism by which the aerosol particle was formed, e.g. condensation of gaseous species on existing nuclei and coagulation of particles.

Aerosol particles play a key role in the earth's atmosphere and influence the climate system, e.g. via their effect on the radiation budget (Boucher et al., 2013). Radiative forcing is a concept to describe the difference of incident solar radiation and energy emitted back to space. Positive radiative forcing would mean that the earth receives more energy than it emits, with a resulting warming effect. Radiative forcing is expressed in Wm^{-2}. Aerosols can influence the radiative forcing by two effects. On the one hand, aerosol particles can scatter and absorb solar radiation. As a consequence, less solar radiation reaches the earth's surface. This is described as the "direct effect" of aerosols. The most common light-absorbing aerosol species are black carbon and mineral dust. On the other hand, aerosol particles act as seed particles for the formation of cloud droplets. Therefore, a change in the aerosol can indirectly influence the radiative properties of the cloud, designated as the "indirect effect" of aerosols (Boucher et al., 2013).

Fig. 2.1.1 shows the radiative forcing for different emitted compounds in the period of 1750 to 2011. The values for aerosols vary a lot and have a large uncertainty, especially for black carbon (Myhre et al., 2013).

2.1.2 Aerosol mechanics

Chapter 2.2 deals with the sampling of aerosols. For a better understanding, it is important to introduce some essential parameters and equations regarding the behaviour of an aerosol particle in a fluid beforehand. A fluid is a substance that continually deforms under external forces, their shear modulus is zero. In physics, all liquids and gases are summarized under this term. Another characteristic property of the fluid is its flow regime. The flow in a fluid can be laminar or turbulent. Laminar flow means that the streamlines are parallel, in contrast to a turbulent flow with streamlines forming eddies. The Reynolds number Re is a characteristic number used to predict the flow regime. The following Eq. 2.1.1 represents the Reynolds number for the flow of a fluid around a particle moving through it. This parameter defines the ratio of inertial to viscous forces in the fluid.

$$Re = \frac{\rho \, D_p \, V}{\eta} \qquad (2.1.1)$$

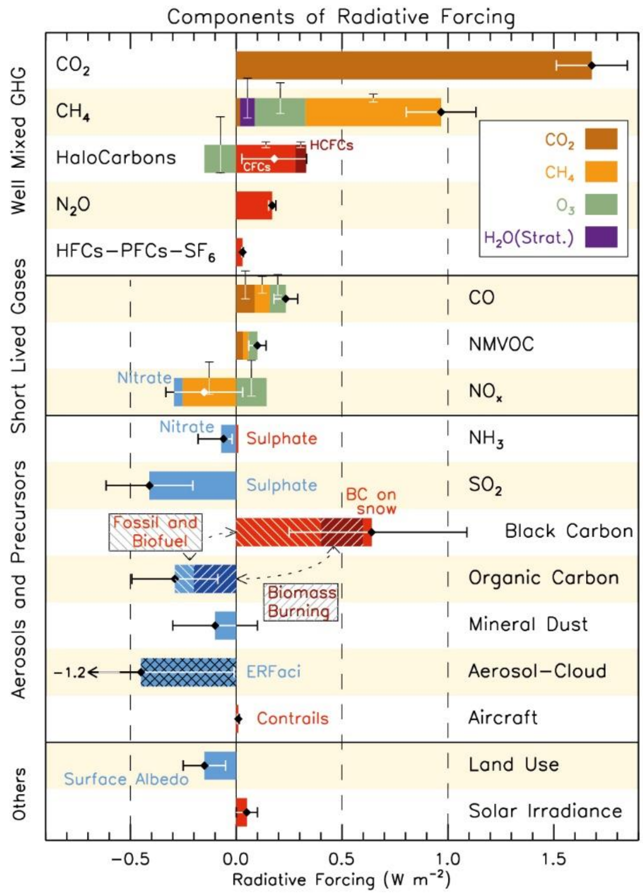

Figure 2.1.1: Radiative forcing of different compounds. Figure adopted from Myhre et al., 2013.

where V is the velocity of the particle relative to the fluid, D_p the particle diameter, ρ the density and η the dynamic viscosity of the fluid. The dynamic viscosity is given by

$$\eta = 1.7188 \cdot 10^{-5} \left[\left(\frac{T}{273.15} \right)^{1.5} \left(\frac{384.15}{T + 111} \right) \right] \tag{2.1.2}$$

where T is the temperature of the fluid (Seinfeld and Pandis, 2006).

For a very small Reynolds number the flow is laminar. On the other hand, a high Reynolds number indicates a turbulent flow.

For the laminar case, the drag force of a spherical particle moving through a fluid can be derived from the Navier-Stokes equation. The derivation requires assumptions of the system, e.g. the inertial forces of the particle are negligible compared to viscous forces, the fluid is incompressible, the velocity of the fluid at the particle's surface is 0. The resulting relationship is called Stoke's law and is defined by

$$F_D = 3\,\pi\,\eta\,V\,D_p \qquad (2.1.3)$$

As mentioned before, one important assumption is that the relative velocity of the fluid is 0 at the particle's surface. This assumption is not correct for small particles with diameters close to the mean free path of the fluid[2]. The result is a "slip" at the surface of the particles and a faster settling in the fluid. To correct Stoke's drag force for this effect, the Cunningham correction factor C_C is considered. It depends on the particle diameter and the mean free path. The mean free path and the Cunningham correction factor can be calculated with

$$\lambda = 0.0651\,\frac{\eta}{1.8 \cdot 10^{-5}}\,\frac{1013}{p}\,\sqrt{\frac{T}{298}} \qquad (2.1.4)$$

$$C_C = 1 + \frac{2\lambda}{D_p}\left[1.257 + 0.4\exp\left(\frac{-1.1\,D_p}{2\lambda}\right)\right] \qquad (2.1.5)$$

where p is the pressure of the fluid (Seinfeld and Pandis, 2006). The reduced Stoke's law becomes

$$F_D = \frac{3\,\pi\,\eta\,V\,D_p}{C_C} \qquad (2.1.6)$$

An important application of the Stoke's law is the derivation of the highest velocity of a particle undergoing gravitational settling. The velocity is reached when the drag force F_D of the particle is equal to the force of gravity F_G and is called terminal settling velocity V_{TS}.

$$V_{TS} = \frac{\rho_p\,D_p^2\,g\,C_C}{18\,\eta} \qquad (2.1.7)$$

where ρ_p is the density of the particle and g the gravitational acceleration.

[2] The mean free path λ characterizes the average distance between collisions of a particle with a molecule of the fluid.

As seen in Eq. 2.1.6, the drag force is directly proportional to the velocity. Therefore, rearranging the Stoke's law gives the particle mechanical mobility B, being the ratio of the particle's velocity and drag force. The terminal settling velocity can now be easily calculated by the product of the mobility B and the external force. The external force can be gravity as seen above, or others like centrifugal or electrical forces.

The product of the particle's mass m with its mobility gives the relaxation time, a useful parameter for understanding the particle's motion. It quantifies the time, required by the particle to adjust to changes in the external force field. The relaxation time can be determined by

$$\tau = mB = \frac{\rho_p \, D_p^2 \, C_C}{18 \, \eta} \tag{2.1.8}$$

It is also defined as the time, a particle needs to reach ≈63% of its terminal settling velocity. Another important parameter, is the maximum distance a particle will move in still air without external forces, called stopping distance. The particle starts to move with its initial velocity V_0 and slows down due to friction with the air. When the velocity of the particle equals V_0/e, it has travelled the stopping distance S. Analogical to the relaxation time, the stopping distance characterizes the ability of the particle to change momentum. The product of the relaxation time and the initial velocity defines the stopping distance S.

The introduction of the relaxation time and the stopping distance allows to raise another powerful parameter in aerosol science, the Stokes number. The Stokes number is a dimensionless number and is defined as the ratio of the stopping distance of a particle to a characteristic dimension of an obstacle L, which occurs in a flow system. The Stokes number Stk is used to characterize inertial impaction and is given by

$$Stk = \frac{S}{L} = \frac{\tau \, V_0}{L} = \frac{\rho_p \, D_p^2 \, C_C \, V_0}{18 \, \eta \, L} \tag{2.1.9}$$

In a flow system where an obstacle occurs, the streamlines of the flow change their directions. The Stokes number can now be calculated with the properties of the aerosol particle and provides information, if the particle can follow the streamlines or not. If this is not the case, the inertia of the particle is too high and the particle will impact on the obstacle. For Stk $\ll$ 1 the particle can follow the streamlines and also changes its direction, for $Stk \gg 1$ the particle can't adjust to the new condition and continues moving in a straight line until it will impact on the obstacle (Hinds, 1999).

Decisive for the Stokes number is the diameter of the particle. For larger particles, the Stokes number increases and the particles more likely tend to impact on the obstacle.

An important application, where the Stokes number plays an essential role for the characterization, is the impactor. In an impactor, the aerosol flows through a nozzle straight to a so-called impactor plate. Instead of the velocity of the particle V_0, the flow velocity u in the impactor is considered. As a characteristic length the half of the nozzle diameter D_N will be taken. The streamlines of the flow split up and change the direction by an angle of about 90°. The Stokes number can be used to determine if the particles can follow the streamlines. Aerosol particles smaller than a certain diameter pass the impactor plate, other remain there. For a full size distribution of an aerosol, a series of impactors needs to be installed. The flow velocity in the different impactors will be increased for every impactor stage and the result is an impaction of aerosol particles with a decreasing size at the different impactor plates. This is known as a cascade impactor and Fig. 2.1.2 shows the schematic setup of such an instrument.

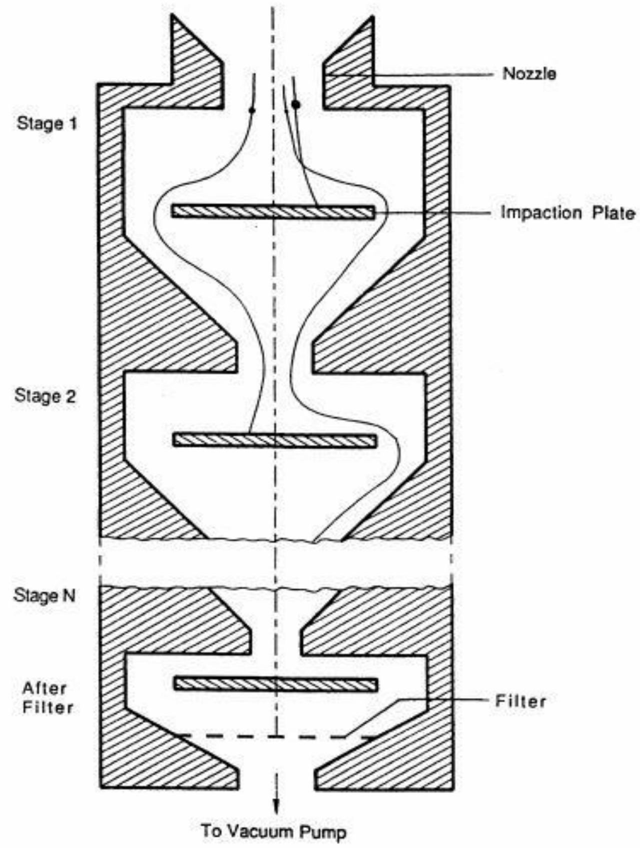

Figure 2.1.2: Schematic setup of a cascade impactor. Figure adopted from Kulkarni et al., 2011.

The Stokes number can also be used to study particle deposition in an aerosol sampling system. For example for an inlet, which is misaligned and not parallel to the ambient aerosol flow. The Stokes number can help to determine, which particles will follow the streamlines into the inlet and which will pass the inlet or impact on the inlet walls, similar to the principle of the impactor.

2.2 Aerosol sampling

In aerosol science it is important to collect aerosol samples and transport them to different measuring instruments. The analysis of these instruments should give a proper representation of the properties of the ambient aerosol. Therefore, it is essential to have a convenient sampling system, consisting of inlets and sampling lines, that ensures that a representative probe of the ambient aerosol enters the instrument.

Fig. 2.2.1 shows a schematic representation of an aerosol measurement. On the top of the figure the original composition of the ambient aerosol is depicted. The aerosol consists of particles with different size, shape and number concentration. On the left side of the figure off-line measurements like sampling with a cassette or microscope analysis are listed. In contrast to that, the right side lists on-line measurements which have a real time resolution of aerosol properties, e.g. number concentration. The sampling efficiency, internal losses or the sensor response of the instruments lead to a distorted composition of the original aerosol, which will be analysed by the instrument.

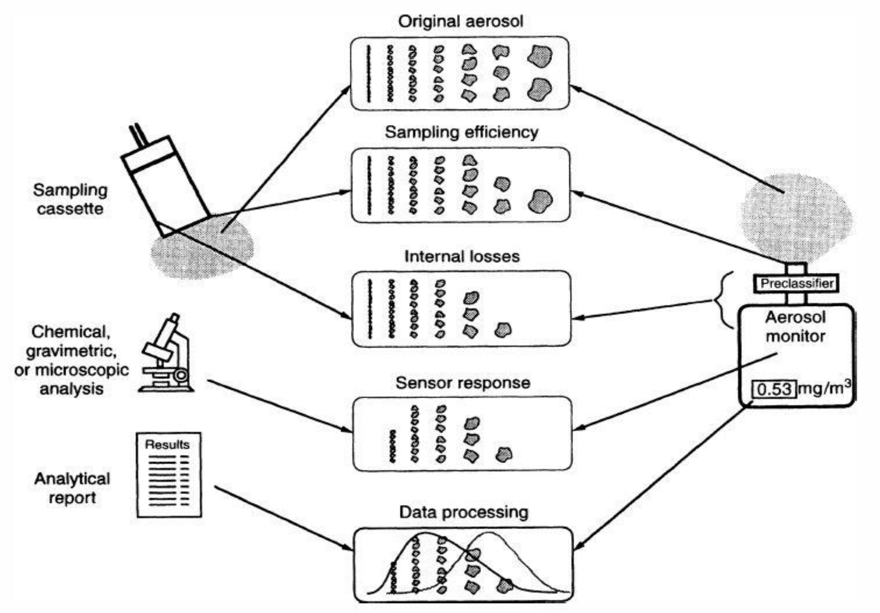

Figure 2.2.1: Schematic representation of an aerosol measurement with different effects that lead to a distorted composition of the original aerosol. Figure adopted from Kulkarni et al., 2011.

In this chapter the overall efficiency of a sampling system will be discussed. The internal losses and the sensor response will be described in chapter 3.2 along the explanation of the main instruments used in this thesis.

An aerosol sampling system normally consists of an inlet followed by sampling lines leading to the instruments (Fig. 2.2.2). The main parameter which characterizes the whole sampling system is the sampling efficiency η_{sample}, which is the product of the inlet efficiency η_{inlet} and the transport efficiency $\eta_{transport}$.

$$\eta_{sample} = \eta_{inlet}\, \eta_{transport} \tag{2.2.1}$$

An efficiency gives the ratio of the concentration of particles of a certain size before and after a certain part of the sampling system. In the following, the inlet efficiency η_{inlet} and the transport efficiency $\eta_{transport}$ will be explained. Theses efficiencies depend on a lot of different parameters, like the geometry of the sampling system and the flow velocities. One of the most important parameters, on which the sampling efficiency is dependent on, is the particle diameter.

An important parameter to characterize the size-dependent transmission efficiency is the so-called cutoff-diameter D_{50}. The cutoff-diameter designates the particle diameter with 50% sampling efficiency, i.e. 50% of the ambient particles of that size pass the inlet and the sampling line and can be detected by an instrument (Hinds, 1999). In most cases, the sampling efficiency is characterized by two different cutoff-diameters. Between those two cutoff-diameters the efficiency is higher than 50%. Outside this range, the efficiency is lower. A value often used to characterize sampling systems is the Stokes number (explained in 2.1.2) Stk_{50} using the cutoff-diameter D_{50}.

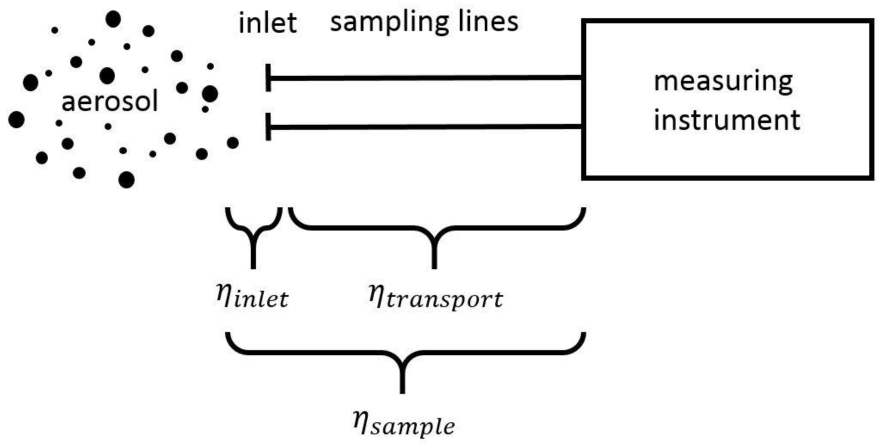

Figure 2.2.2: Schematic representation of an aerosol sampling system.

2.2.1 Particle sampling efficiency at inlets

The inlet efficiency η_{inlet} is the product of the aspiration efficiency η_{asp} and the transmission efficiency η_{trans}.

$$\eta_{inlet} = \eta_{asp}\, \eta_{trans} \tag{2.2.2}$$

These two components are dependent on the sample velocity U through the inlet, the geometry, the size and position of the inlet and the particle diameter. It can also be influenced by the free-stream gas velocity U_0, this implies that the considered area for the efficiency already starts outside the inlet respectively the sampling system. The aspiration efficiency η_{asp} is the fraction of the concentration of aerosol particles that enter the inlet compared to the concentration of aerosol particles in the ambient gas surrounding the inlet. The transmission efficiency η_{trans} is the fraction of the aspirated particles transmitted to the rest of the sampling system, e.g. the sampling lines, leading to the instruments. This efficiency can be split up into efficiencies caused by inertial deposition and gravitational settling.

The first distinction made, regarding this efficiency, is the alignment of the inlet respectively its nozzle. When the nozzle, and so the flow inside the sampling line, is parallel to the flow of the ambient gas stream, the sampling is called isoaxial. When the two flows are not parallel, the case is called anisoaxial or nonisoaxial.

2.2.1.1 Isoaxial sampling

Assuming isoaxial sampling, the next distinction is made in respect to the velocities of the flow inside the sampling line U and the free-stream gas velocity U_0. When both velocities are equal ($U = U_0$), the sampling is called isokinetic. In this case the aspiration efficiency is 1 and transmission losses could only be caused by gravitational settling. As a result of the gravitational settling, the particles deposit on the inside wall of the inlet. This effect is characterized by the gravitational deposition parameter Z:

$$Z = \frac{L\, V_{TS}}{U\, d} \tag{2.2.3}$$

The gravitational deposition parameter Z depends on the inlet region length L, the terminal settling velocity of the aerosol particle V_{TS}, the flow velocity inside the sampling line U and the nozzle diameter d. The transmission efficiency depends on a correlation of the Stokes number based on the ambient gas velocity Stk, the inlet Reynolds number Re and the gravitational deposition parameter Z and is given by

$$K = Z^{1/2}\, Stk^{1/2}\, Re^{-1/4} \qquad (2.2.4)$$

For a high transmission efficiency, K should be low. Another reason for transmission losses could be a free-stream turbulence. For aerosol sampling, the isokinetic configuration is the ideal one with the highest efficiency to carry aerosol with a wide range of particles with different diameters to the sampling lines.

The sampling is called sub-isokinetic, when U_0 is greater than U ($U < U_0$). This condition leads to an aspiration efficiency equal to or greater than 1, up to the limit of the ratio U_0/U for larger particles. The streamlines of the ambient flow must diverge into the nozzle which could result to an enrichment of larger particles. Transmission losses can be caused by gravitational settling, free-stream turbulence and inertial impaction due to expanding streamlines.

When the flow velocity in the ambient gas is smaller than in the inlet ($U > U_0$), the sampling is called super-isokinetic. The streamlines of the ambient free-stream flow have to converge into the nozzle, the depletion of larger particles could be the result. Here, the aspiration efficiency is 1 or smaller, decreasing to a limit of the ratio U_0/U for larger particles. In this case, the transmission losses are caused by gravitational settling, free-stream turbulence and turbulent deposition due to the constriction of the ambient flow stream.

For the sub-isokinetic and the super-isokinetic case the transmission efficiency caused by inertial deposition depends on the Stokes number based on the free-stream ambient gas velocity and the nozzle diameter. By keeping the Stokes number small a high transmission efficiency is given.

2.2.1.2 Anisoxial sampling

Considering the anisoxial sampling, an important parameter is the sampling angle Θ. This is the angle between the direction of the flow inside the nozzle and of the ambient free-stream. As a result, the streamlines of the ambient free-stream flow have to bend to the inlet. In addition to the effects that can cause particle losses for the isoaxial sampling another deposition mechanism occurs. Particles with a high inertia can’t follow the streamlines into the nozzle and impact on the walls of the inlet. When Stk < 0.01 the particles can follow and the loss is negligible (Hinds, 1999).

Sometimes misaligned inlets were used deliberately to sample aerosol particles with a certain size. Therefore it is important to know the inlet's size dependent efficiency. The equations of the efficiencies for the isoaxial sampling are no longer valid for this case. The correlation K (Eq. 2.2.4) is now given by

$$K_\theta = K\sqrt{\cos\theta} \qquad (2.2.5)$$

For a sampling angle of 0°, K doesn't change and the sampling is isoaxial. When the inlet is aligned horizontal and $\theta = 90°$, K_θ equals 0 and there are no losses due to gravitational settling

Figure 2.2.3 shows the overall inlet efficiency as a function of the Stokes number. The inlet efficiency is calculated for different sampling angles Θ and ratios of the velocities of the free-stream flow and the flow inside the inlet. As seen in the figure, an inlet efficiency of 1 is permanently given in the case of isokinetic sampling. This means that it is the best case to get a representative sample of aerosol and that the aerosol is not affected in any way by the sampling process in the inlet.

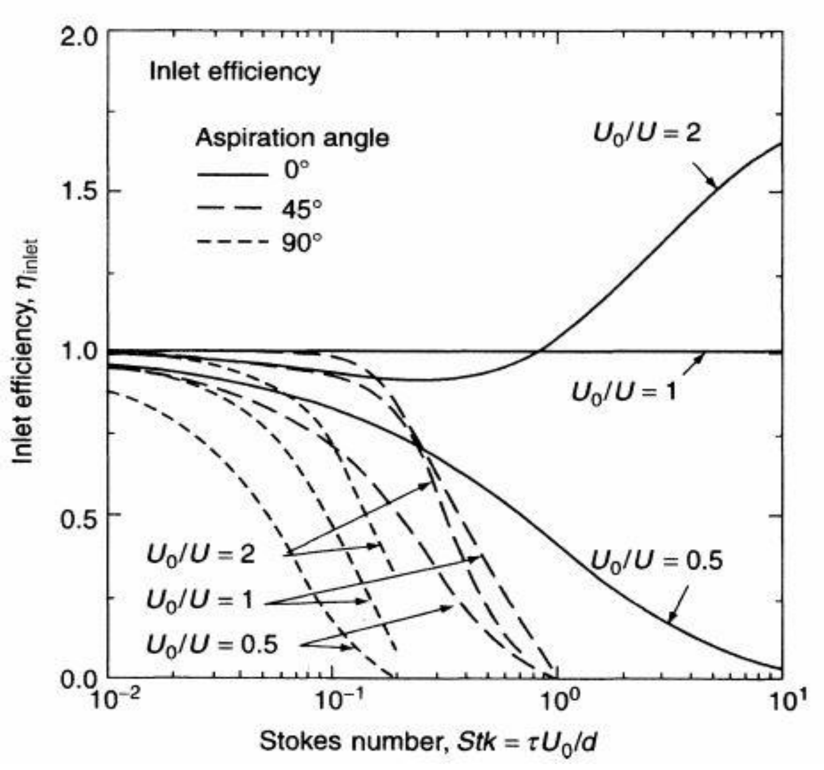

Figure 2.2.3: The inlet efficiency for different configurations as a function of the Stokes number. Figure adopted from Kulkarni et al., 2011.

2.2.2 Particle transport efficiency through sampling lines

Once the aerosol has passed the inlet, it must be carried to the instruments. This happens with sampling lines. Sampling lines have typically bends and constrictions which potentially result in particle losses.

A turbulent flow inside can also lead to losses. If the flow in the sampling lines is laminar or turbulent, can be determined with the sampling line flow Reynolds number Re:

$$Re = \frac{\rho_g\ U\ d}{\eta} \tag{2.2.6}$$

where U is the velocity of the flow, d the inner diameter of the sampling line, ρ_g the density and η the viscosity of the gas. The following equations of the efficiencies for the different mechanisms are valid for the laminar case (Re < 2000) or the turbulent case (Re > 4000) (Kulkarni et al., 2011). For the transition regime (2000 > Re > 4000) there aren't any equations available.

The most common deposition mechanisms that lead to losses, are listed below (Kulkarni et al., 2011):

- Gravitational settling
- Diffusional settling
- Turbulent inertial deposition
- Inertial deposition at a bend
- Inertial deposition at flow constrictions
- Electrostatic deposition
- Thermophoretic deposition
- Diffusiophoretic deposition

The transport efficiency $\eta_{transport}$ is the product of the efficiencies in each section of the sampling line for each mechanism:

$$\eta_{transport} = \prod_{section} \prod_{mechanism} \eta_{section,mechanism} \tag{2.2.7}$$

The mechanisms will be explained in this chapter. For the precise equations for the efficiencies of each mechanism the interested reader is referred to Kulkarni et al. (2011).

2.2.2.1 Particle deposition

Gravitational settling: For non-vertical sampling lines, gravitational settling respectively sedimentation of aerosol particles due to gravitational forces can occur. Particles with a diameter larger than 500 nm are mostly affected by this deposition mechanism and as a result they could settle on the lower wall of the sampling line. In a vertical sampling line the transport efficiency for this mechanism is 1. For the calculation of the efficiency the gravitational deposition parameter Z from Eq. 2.2.3 can be used. As for the inlet efficiency, Z should be small to guarantee a high efficiency. For an inclined or vertical aligned sampling line the gravitational deposition parameter is multiplied with the cosine of an inclination at an angle θ, similar to the correlation of Eq. 2.2.5. Figure 2.2.4 shows the transport efficiency as a function of the gravitational settling parameter.

Diffusional settling: Particles are undergoing Brownian motion and diffuse from regions with high concentration to low particle concentration. Highly affected by this are particles smaller than 100 nm. The walls of the sampling lines acts like a sink for those particles. The efficiency of this mechanism depends on the diffusion coefficient D. D can be computed by

$$D = kTB \tag{2.2.8}$$

where k is the Boltzmann constant, T the temperature and B the particle mobility. In a sampling line with a laminar flow the transport efficiency can be described with an exponentially decreasing function. The function only depends on the parameter $\xi = \pi DL/Q$ with the sampling line length L and the volumetric flow Q. This parameter should be kept small to ensure a high transport efficiency.

Turbulent inertial deposition: The larger the particle, the greater is the chance that the particle gets lost because of inertial deposition in a turbulent flow. Because of the high inertia, the particle can't follow the curvy streamlines. The transport efficiency of the deposition mechanism can be described as an exponentially decreasing function. It depends on the quotient $\pi D_p L V_t/Q$, where Q is the volumetric flow, L the inner diameter of the sampling line, D_p the particle diameter and V_t the experimentally determined turbulent inertial deposition velocity. V_t can be calculated using the following empirical formula (see Kulkarni et al., 2011):

$$V_t = \frac{U\left(6\cdot 10^{-4}\left(0.0395\,Stk\,Re^{3/4}\right)^2 + 2\cdot 10^{-8}\,Re\right)}{5.03\,Re^{1/4}} \tag{2.2.9}$$

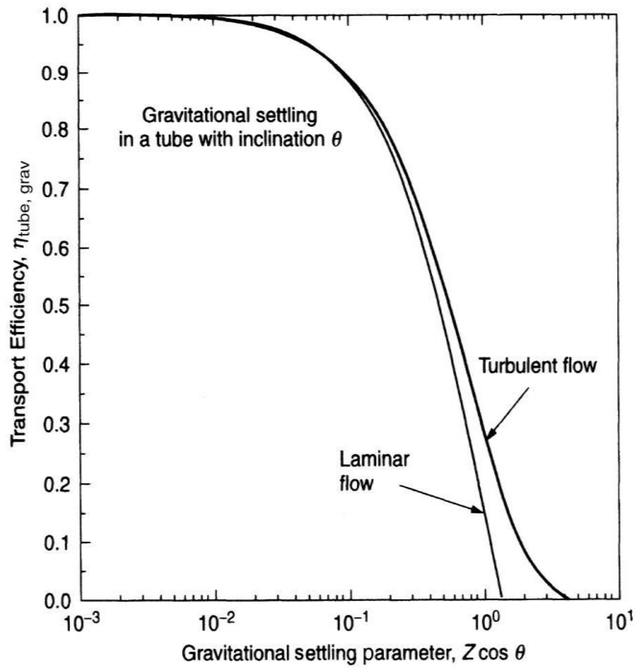

Figure 2.2.4: The transport efficiency for laminar and turbulent flow as a function of the gravitational settling parameter. Figure adopted from Kulkarni et al., 2011.

Inertial deposition at a bend: In bends of sampling lines the flow changes its direction and this leads to a loss of large particles that can't follow the flow and deposit on the walls of the sampling line. This loss can be described with the Stokes number and the bend angle ϕ of the sampling line. For an increasing Stokes number or bend angle, a decreasing transport efficiency is the result. A sampling system should have as little bends as possible.

Inertial deposition at flow constrictions: Another reason for particle loss are sampling line constrictions. Like in a bend, large particles can't follow the streamlines and deposit on the sampling line wall. If the following tubing enlargement is not smooth, turbulent flow inside the sampling line and particle losses could be the result. For this effect no equations characterizing the losses are available (von der Weiden et al., 2009).

Electrostatic deposition: The loss of charged aerosol particles due to electrostatic forces can occur in sampling lines. This effect is negligible when the sampling line walls are grounded and consist of conductive material. If this is the case, the sampling line walls form a Faraday cage and no electrostatic forces affect the aerosol particle and there is no additional deposition in the sampling lines.

Thermophoretic deposition: A temperature gradient in the sampling line can result in the loss of aerosol particles. This is effect result from the difference in momentum of the air molecules. On the warmer side, the air molecules have a higher momentum and transfer more momentum to the aerosol particles than on the colder side. Therefore, the particles shift from higher to lower temperatures. In the most cases, the aerosol is warmer than the sampling line wall. When the temperature difference is not higher than 40 K the particle loss due to this effect is negligible (von der Weiden et al., 2009).

Diffusiophoretic deposition: Due to concentration gradients, aerosol particles can deposit on the sampling line walls. If the sampling probe is well mixed and the temperature gradient between sampling line and aerosol is small, this effect does not influence the transport efficiency (von der Weiden et al., 2009).

A useful tool for calculating the sample efficiency and the particle losses due to the sampling system setup, is the particle loss calculator (PLC; von der Weiden et al., 2009). By entering all important properties of the sampling system, the PLC will calculate the efficiency function in dependency of the particle diameter by using the equations mentioned above. The calculator provides a quick way to get a sense of the losses in the sampling system and helps to correct measured aerosol particle concentrations. It allows to calculate transport efficiencies of all the previous explained mechanisms except of electrostatic, thermophoretic and diffusiophoretic deposition.

2.3 Aerosol size distribution

As mentioned in chapter 2.1.1, the size of an aerosol particle is a key parameter to characterize its behaviour. An aerosol which consists only of particles with the same size is called monodisperse aerosol. There are different technological processes which can generate particles of a single size and can be used in the laboratory, e.g. for calibrating measuring instruments. Most aerosol in the atmosphere are a mixture of particles with different diameters. Potentially originating from different source processes and these mixtures are then called polydisperse aerosols. As seen in Fig. 2.3.1 aerosol particles cover a large range of diameters which can span several orders of magnitude. For this, it is important to find appropriate statistical values and parameters to characterize a measured size distribution in a proper way. The process of getting these values will be introduced in this chapter.

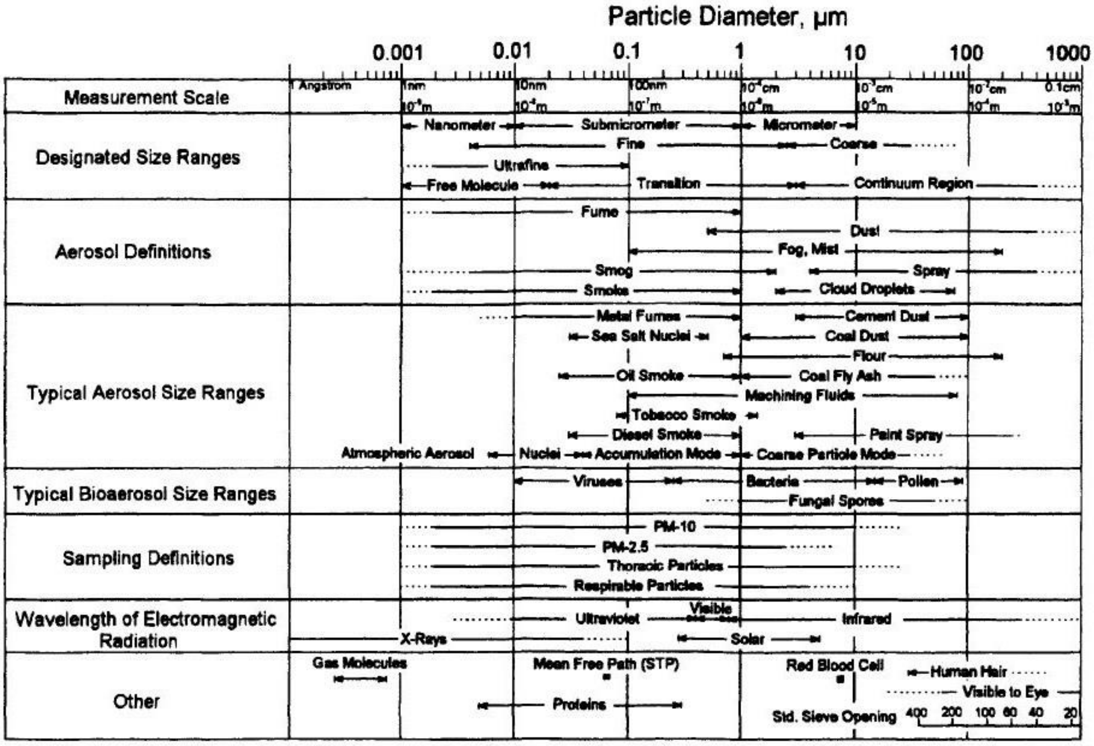

Figure 2.3.1: Size ranges of particles and their definitions. Figure adopted from Hinds, 1999.

2.3.1 Properties of an aerosol size distribution

In aerosol science, a lot of different instruments to measure size distribution, are available. For now, to get a full understanding of a size distribution, it's not important to know the measuring method of the instrument and how the size distribution is identified. The measuring principle of the used instrument will be discussed in chapter 3. For this example we imagine a set of aerosol particles with a different size and a total number of particles N.

The first step to get a good overview of the particles is to divide the whole size range into a series of size intervals. The size intervals should be continuous and non-overlapping. The widths of the intervals can be denoted with $\Delta D_{p,i}$. D_p is defined as the particle diameter, normally given in µm, and the subscript i for the i-th interval. All the aerosol particles can now be sorted into those intervals respectively bins and the outcome is a histogram of grouped data of counts ΔN_i, within the previous defined bins.

In this way, the bin counts are not really comparable because the width of the bins are maybe not equal over the whole size range. It is recommended to normalize the bin counts ΔN_i by the bin width $\Delta D_{p,i}$. n_i (Eq. 2.3.1) is then the height of the normalized rectangle of the i-th bin and gives an area equal to the number of particles in this bin in the unit counts per µm.

$$n_i = \frac{\Delta N_i}{\Delta D_{p,i}} \tag{2.3.1}$$

The total number of particles N is then given by

$$N = \sum n_i \, \Delta D_{p,i} \tag{2.3.2}$$

For a further comparison of size distribution shapes, it is recommended to normalize the histogram by the total number of particles N. Now the height of the rectangles n_i' gives the fraction of particles in the size bin i and the sum of all of those fractions multiplied with the bin widths equal 1.

The important next step for a precise size distribution with full information is to move from the histogram to a smooth curve by reducing the bin widths to infinitesimal sizes. This leads to the so-called probability density function (PDF) $f(D_p)$, giving the frequency probability for a certain particle diameter.

The fraction of the total number of particles df having diameters between D_p and $D_p + dD_p$ is now

$$df = f(D_p) \, dD_p \tag{2.3.3}$$

with $f(D_p)$ as the PDF. Multiplying Eq. 2.3.3 by the total number of particles N it turns into

$$dN = n(D_p) \, dD_p \tag{2.3.4}$$

with dN as the number of particles in the size interval and $n(D_p)$ as the number distribution function. This expression is mostly used in aerosol science in relation to size distributions. Usually the unit of dN is not only considered as counts as in Eq 2.3.4, but rather counts per cubic centimetre. The reason for this is, that most of the measuring instruments which were used to detect the size of particles have a sample flow. This sample flow can vary through the different instruments. For a better comparability and to avoid discrepancies the volume of the sample probe is always considered in size distributions.

By calculating the integral of the PDF in a certain range from diameter a to diameter b gives the fraction f_{ab} of particles in that range. Furthermore, the integral from 0 to infinity of the PDF equals 1 because it covers all particles. Besides that, the integral from 0 to a certain particle diameter a gives the cumulative fraction F of particles smaller than a (Eq. 2.3.5).

$$F(a) = \int_0^a f(D_p) dD_p \tag{2.3.5}$$

The advantage of the PDF is that it introduces some descriptive statistical parameters, which characterizes a size distribution. The most commonly used values are different averages: the arithmetic mean, the count and the modal diameter.

The count mean diameter $\overline{D}_p$ is the sum of all the particle diameters divided by the total number of particles or the integral like in the following equation (2.3.6).

$$\overline{D}_p = \frac{\sum D_p}{N} = \int_0^\infty D_p \, f(D_p) \, dD_p \tag{2.3.6}$$

The count median diameter, called CMD, is the diameter for which 50% of the total number of particles are smaller:

$$F(CMD) = 0.5 \tag{2.3.7}$$

The count modal diameter D_{mod} is the most frequent diameter of the ensemble of particles. So at this diameter the size distribution reaches its maximum. D_{mod} can be derived by setting the derivation of the PDF to zero:

$$f(D_{mod}) = \max\{f(D_p')\} \Rightarrow D_p' = D_{mod} \tag{2.3.8}$$

For a symmetrical distribution all three diameters have the same value, for an asymmetrical distribution this is not the case. For a distribution with a long tail toward larger particle diameters, the count mean diameter is the biggest, followed up by the count median and the count modal diameters as the smallest. For a distribution with a long tail towards smaller particle diameters, it's the other way round.

Other important parameters of a size distribution are the variance σ^2 and the geometric mean diameter D_g ,they can be calculated with the following equations 2.3.9 and 2.3.10.

$$\sigma^2 = \int_0^\infty (D_p - \overline{D}_p)^2 f(D_p)\, dD_p \tag{2.3.9}$$

$$D_g = (D_{p,1} \cdot D_{p,2} \cdot \ldots \cdot D_{p,N})^{1/N} \tag{2.3.10}$$

2.3.2 Lognormal distribution

As mentioned before, particle sizes can span a size range of four orders of magnitude. In addition, size distributions are in the most cases not symmetrical. For a better visualisation of size distributions, a logarithmic representation in particle diameter is preferable. For that, a transformation of the size variable $f\,(D_p) \Rightarrow f\,(\log_{10} D_p)$ is required. Because of the impossibility of taking the logarithm of a dimensional variable, the logarithm will be taken to a reference size of 1 µm, so $D_p \Rightarrow \log_{10} D_p \equiv \log_{10}\left(\frac{D_p}{1\mu m}\right)$. Eq. 2.3.3 and 2.3.5 change then to

$$df = f(log_{10} D_p)\, dlog_{10} D_p \tag{2.3.11}$$

$$F(a) = \int_{-\infty}^{log_{10} a} \frac{df}{dlog_{10} D_p}\, dlog_{10} D_p \tag{2.3.12}$$

Another advantage of this logarithmic transformation is that it has been shown semi-empirically that many naturally occurring aerosols can be described by a superposition of lognormal distributions. A lognormal distribution is similar to a normal distribution, like the Gaussian distribution, only using logarithmic variables. The PDF and the number distribution function can be expressed in the following way

$$\frac{df}{dlog_{10}D_p}N = \frac{dN}{dlog_{10}D_p} = \frac{N}{\sqrt{2\pi}\, log_{10}\sigma_g} \exp\left(\frac{-(log_{10}D_p - log_{10}CMD)^2}{2(log_{10}\sigma_g)^2}\right) \quad (2.3.13)$$

The only two parameters which are used in the lognormal distributions and completely defines it, are the count median diameter CMD, being the centre of the distribution, and the geometric standard deviation σ_g. The standard deviation can be calculated in the following way

$$\sigma_g = \left(\frac{\sum(D_p - D_g)^2}{N}\right)^{\frac{1}{2}} \quad (2.3.14)$$

The benefit from using the lognormal distribution is to easily determine probability diameters of the distribution. For a normal distribution, the range $\mu \pm \sigma$ covers 68.27% of the integral of the distribution, with μ characterizing the centre of it. The particle diameters defining this range are called the 16th and 84th percentiles. For the lognormal distribution these percentiles can be calculated as following

$$log_{10}D_{p,16\%} = log_{10}CMD - log_{10}\sigma_g \quad (2.3.15)$$

$$log_{10}D_{p,84\%} = log_{10}CMD + log_{10}\sigma_g \quad (2.3.16)$$

2.3.3 Moment distribution

So far, only the probability density function based on the number distribution was discussed. Sometimes in aerosol science it is important to consider other properties of the aerosol like particle surface or volume, instead of looking at the number distribution function, which leads to the overall term of moment distributions. The 0th moment gives the already discussed number distribution, the 2nd and 3rd moment gives the surface and volume distribution. The surface and volume density function f_S and f_V can be derived from Eq. 2.3.3.

$$f_S(D_p) = \pi D_p^2 \, f(D_p) \tag{2.3.17}$$

$$f_V(D_p) = \frac{\pi}{6} D_p^3 \, f(D_p) \tag{2.3.18}$$

$f_S(D_p)$ and $f_V(D_p)$ are the PDF for surface and volume of particles in the diameter range between D_p and $D_p + dD_p$ assuming spherical particles. These functions give the fraction of surface and volume in this size range in respect to the total surface and volume. Sometimes instead of the volume probability function, the mass probability function is used, where the density of the particles is considered as well.

As seen in Fig. 2.3.2, the peaks of the PDF's for the different moments are shifted. The number size distribution is dominated by smaller particle compared to the volume moment, where larger particles play a key role.

Like for the number size distribution, different averages can be calculated for the surface and volume distribution. This gives the surface mean, median and modal diameter and, normally calculated for mass, the mass mean, median and modal diameter.

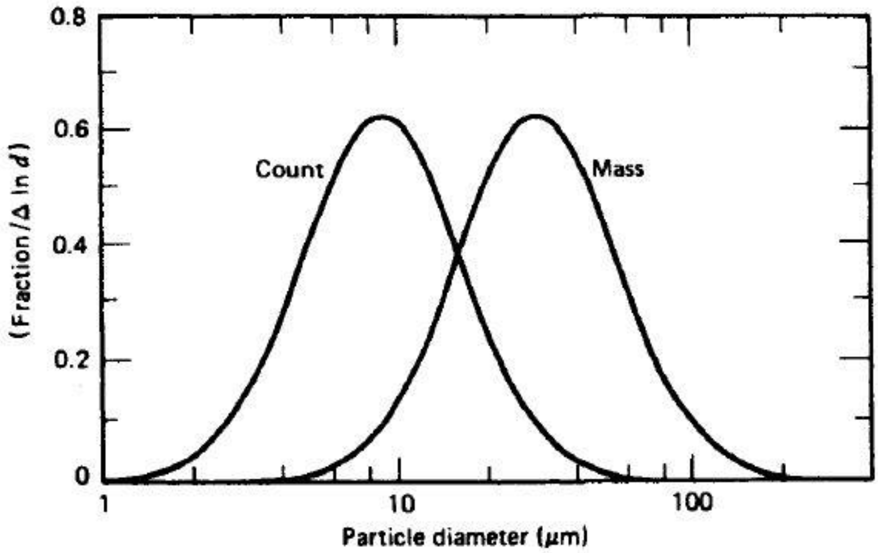

Figure 2.3.2: Number (count) and mass distribution in a logarithmic representation. Figure adopted from Hinds, 1999.

Chapter 3

Methods

The following chapter starts with an overview of the A-LIFE project and covers all the measurements and instrument settings relevant for this thesis. Section 3.2 deals with the two most important instruments used in this work, the (Grimm) SkyOPC and the Cloud and Aerosol Spectrometer (CAS). An explanation and the working principle of these instruments is given. At the end of this chapter a description of the calibration and calculation of the number size distribution of the SkyOPC is given, based on Walser et al., 2017.

3.1 A-LIFE project

The A-LIFE project has the aim to investigate absorbing aerosols, in particular mineral dust and black carbon. The goal is to characterize the aging and mixing of these aerosols during their lifetime, to assess their contribution to the radiative forcing in mixed aerosol layers, to implement complex particle morphologies in radiative forcing estimates and to investigate potential links between the presence of these particles, aerosol layer lifetime and removal[3].

To achieve these aims, aerosol data were collected in the Eastern Mediterranean. This place is appropriate for this project because it acts like a melting pot of different kinds of aerosols. As seen in Fig. 3.1.1, aerosols from different sources are transported to this area (Dogan et al., 2008). This includes dust from Arabia and from the Sahara, sea salt, and anthropogenic and fire smoke originating in Europe.

The aerosol data were collected at a ground-based station and with the DLR research aircraft Falcon 20-E5 (D-CMET). The airborne measurement campaign was carried out from the 3rd to the 30th of April 2017 and was based at Paphos in Cyprus. At the ground-based station aerosol in-situ, lidar and sun photometer measurements were performed. The airborne measurements with the Falcon were planned depending on the meteorological conditions. The flight planning considered information of the weather forecasts, the forecasted aerosol distributions and of the ground-based measurements.

[3] A-LIFE (2017). Available at: www.a-life.at (Accessed: 1 February 2019)

Figure 3.1.1: Map of the Eastern Mediterranean on the 27th of April in 2017. Source: NASA Worldview

22 research flights were performed with the Falcon including 2 test flights on the 28th and 31st of March 2017 and 4 transfer flights, with a total amount of about 80 flight hours. Tab. A.2 shows an overview of all A-LIFE flights. The nomenclature for the flights are defined as the date in the format yymmdd followed by a or b defining the flight order on that day. For the airborne measurements, instruments were installed in the aircraft cabin and under the wings. The complete instrumentation is summarized in Tab. A.1. The data of the instruments provide a lot of different properties of the aerosol, like size distribution, volatility, scattering and absorption coefficient and refractive index. The size of the aerosol particles was measured in the range from 4 nm up to 930 µm. The implemented instrumentation setup also allowed for detection of the mass and mixing state of black carbon and the concentration of cloud condensation nuclei. Impactors were installed to collect aerosol for later offline analysis.

3.1.1 Falcon aerosol inlet

For the instruments, which were installed inside the aircraft cabin, an aerosol inlet and sampling lines are required. To measure a representative aerosol sample the inlet of the Falcon extends beyond the aircraft boundary layer in order to avoid disturbance of the sampled air by the aircraft fuselage (Weinzierl, 2008). The speed of the Falcon can reach up to 200 m/s relative to the ambient air, called True Air Speed (TAS). As described in the previous chapter the best sampling efficiency can be realized within isokinetic conditions. This means that the incoming air has to be slowed down because of the much lower flow velocity inside the sampling lines to the instruments. Fig. 3.1.2 shows the aerosol inlet of the research aircraft. It consists of three different inlets: forward-facing, sideward-facing and one with a backward orientation. For the A-LIFE field campaign the forward-facing and the sideward-facing inlet were used. The former allows near-isokinetic sampling. The isokinetic conditions are accomplished by a diffusor, a widening tube, where the flow of the ambient air is decelerated (Fiebig, 2001). In the following, this inlet will be mentioned as isokinetic inlet. The sideward-facing inlet, in the following described as sideward inlet, samples non-isokineticly. During the A-LIFE field experiment the flow velocity in the sampling lines behind the isokinetic inlet was 18.67 m/s and 7.32 m/s behind the sideward inlet.

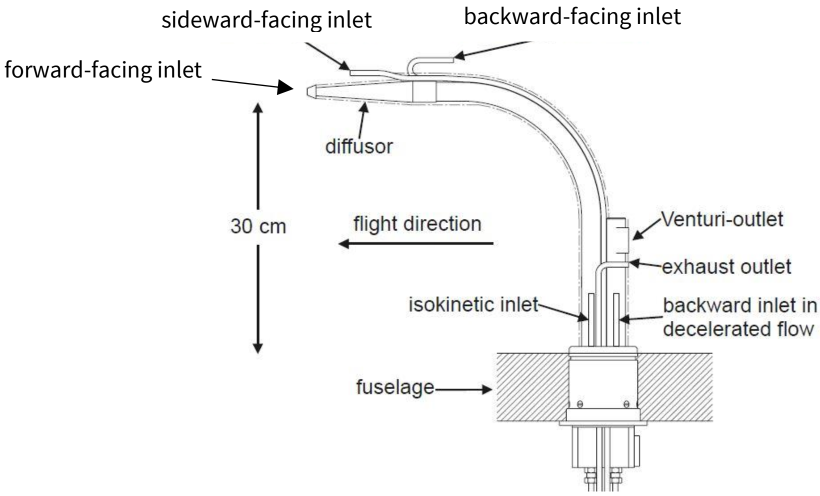

Figure 3.1.2: Aerosol inlet of the Falcon. Figure adopted from Fiebig, 2001.

Most of the in-cabin instruments were connected to the isokinetic inlet except one of two Tri-color Absorption Photometer (TAP), which was connected to the sideward inlet during the whole measurement campaign.

3.1.2 CCNC inlet system

The CCNC is an instrument that allows to study aerosol droplet activation at defined water vapor saturations (Roberts and Nenes, 2005; Lance et al., 2006). In the airborne setup, the CCNC pressure is held constant at $\mathrm{p} \approx 500$ hPa. To ensure that, a Constant Pressure System (CPS), composed of two critical orifices, a pressure-controlled bypass flow circuit including a pump, a pressure gauge and a control valve, is used. At these orifices a sudden tubing contraction occurs and the air flow experiences a pressure drop. The bypass flow circuit regulates this flow for varying ambient pressures such that the pressure behind the orifices stays constant (Walser, 2017). The small aperture orifice was utilized for altitudes z ≈1.7 km respectively for an ambient pressure of $p_{amb} \approx 820$ hPa. For an altitude of z ≈ 1.7 km ($p_{amb} \approx 820$ hPa) the large aperture orifice was used. A constant CCNC pressure with the large aperture orifice could be achieved up to an altitude of $\mathrm{z} < 4.5$ km.

3.2 Main instruments

3.2.1 SkyOPC

Crucial for this thesis work were several Optical Particle Counters (OPCs). During the A-LIFE field campaign two Grimm SkyOPC 1.129 (OPC1 and OPC2) were installed inside the aircraft cabin.

One SkyOPC was connected to the isokinetic inlet during the whole field campaign. In the following this SkyOPC will be named OPC1. The other one was mainly connected to the isokinetic inlet measuring the non-volatile aerosol fraction behind a thermodenuder (TD). The thermodenuder consists of heated tubes with a temperature of 250°C. The volatile components like organic carbon, sulfuric acid, ammonium sulfate and bisulfate evaporate in the heated aerosol. This allows to measure the non-volatile aerosol with the second SkyOPC, named OPC2.

The basic principle of this instrument is the scattering of light. The aerosol enters the instrument perpendicular to the laser beam and is focused to the center of the sampling volume. In the chamber a monochromatic laser with a wavelength of 655 nm is installed. The laser illuminates the aerosol particles and as a consequence, light is scattered by the particles. From a mirror, the scattered light comes to a detector where the light signal is transformed into a voltage signal. This signal is directly proportional to the instrument-specific particle scattering cross section. The cross section is a function of the particle diameter. According to the amplitude of the voltage signals, the OPC counts and sorts them into bins with certain amplitude thresholds. The outcome of the measurement is a histogram.

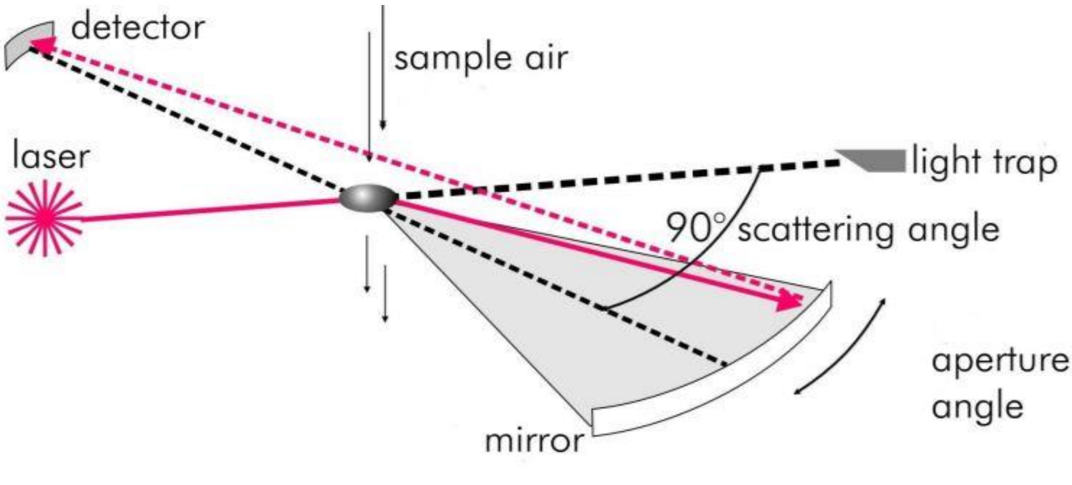

Figure 3.2.1: Schematic working principle of the Grimm SkyOPC 1.129. Figure adopted from Grimm SkyOPC operator manual.

For A-LIFE, the two Grimm SkyOPC 1.129 were utilized with 16 predefined bins and were operated with a 1 Hz sampling frequency. The instrument detected particles in a size range from 250 nm up to about 3 µm. The working principle of an OPC is depicted in Fig. 3.2.1.

3.2.2 Cloud and Aerosol Spectrometer (CAS)

The Cloud and Aerosol Spectrometer (CAS) is one of two parts of the Cloud, Aerosol and Precipitation Spectrometer (CAPS), an instrument consisting of an aerosol spectrometer (CAS, 0.51 – 50 µm) and a cloud imaging probe (CIP, 15 – 930 µm). The device was mounted under the wing of the Falcon. The CAS is a passive inlet OPC (Baumgardner et al., 2001) and has an open pipe in which the optics is located. The ambient air flows through this tube during a research flight. The measurement technique is similar to the Grimm SkyOPC 1.129: the aerosol particle scatters light from an incident laser, an optics system collects the scattered light and guides it to a detector. The detector transforms the pulses into voltage signals.

The instruments detects aerosol particles with diameters from 510 nm to 50 µm. The CAS data was processed and preliminary number size distributions used in this thesis were provided by Maximilian Dollner, University of Vienna.

3.3 Data evaluation

3.3.1 Pre-Processing of the OPC data

Before the SkyOPC data can be used for the calculation of the number size distribution, pre-processing was required. The instruments on the Falcon receive the aerosol sample from different sampling lines. As the length of the sampling lines varies, it is recommended to introduce a general time stamp. The general time stamp can be used as a reference and helps to consider the time offset for every instrument on the Falcon. With the use of the time offset it can be ensured that the same aerosol probe is considered. Longer sampling lines mean that the aerosol has to travel a longer way and this results in a higher time offset. The timestamp of the SkyOPC data was corrected for tubing length with CAPS time being the reference time. The CAPS was chosen as the reference instrument because of its non-inlet setup. By comparing significant peaks of the total number concentration with the CAPS data in a time series, the time offset for both SkyOPCs was defined. The gap between two peaks was considered as the time offset. For OPC1 the time offset was determined to be between 3 and 5 seconds on average. In contrast, a time offset of 6 to 9 seconds was determined for OPC2 as a consequence of the longer sampling lines.

To make sure that the OPC data are comparable, the measured concentrations were corrected to standard temperature and pressure (STP). The so-called STP factor was calculated with a reference temperature of 273.15 K and a reference pressure of 1013.25 hPa.

The recorded concentration of the OPC, detected at an ambient temperature T and an ambient pressure p, was multiplied with the STP factor to report data for standard conditions

$$f_{STP} = \frac{p_{STP}}{p} \cdot \frac{T}{T_{STP}} = \frac{1013.25}{p} \cdot \frac{T}{273.15} \tag{3.3.1}$$

Furthermore, flight sequences in which the Falcon flew through clouds were not considered in this thesis work in order to avoid artefacts at the aerosol inlet.

3.3.2 Number size distribution retrieval

As stated in the previous section, the particle scattering cross section is a function of the particle diameter. Meaning that every particle can be sorted in the associated bin. Indeed, the scattering cross section is a non-monotonic function of particle diameter leading to a distorted sorting of the detected particles by the OPC (Szymanski and Liu, 1986). The desired information for Eq. 3.1.1, the number size distribution (NSD), can be calculated for the OPC from an inversion of a set of so-called Fredholm integral equations of the first kind

$$N_i = \int_0^\infty \kappa_i(D_p)\, n(D_p)\, dD_p \tag{3.3.2}$$

with the number of particles N_i counted in bin i, the corresponding kernel function $\kappa_i(D_p)$ giving the probability for each particle diameter D_p to be sorted into bin i and the NSD $n(D_p)$ (Walser et al., 2017). For a precise NSD the characterization and definition of the kernel function is important. The kernel function requires information of the OPC bin threshold voltages and the linear relationship between the particle cross section and the signal voltages, and the relationship between scattering cross section and particle diameter (Walser et al., 2017).

With the geometry of the OPC and the properties of the used laser inside the OPC, the scattering cross section $\tilde{C}_{scat,m}$ of a spherical particle with diameter D_p and refractive index m can be calculated by means of Mie theory. The refractive index depends on the material of the particle and can be described with a complex number. The imaginary part of the complex number characterizes the ability of the particle to absorb light. For an imaginary part of zero, the particle doesn't absorb any light.

An ideal OPC would detect the light, scattered by the aerosol particles, as a sharp distribution of signal peak voltages U_m. U_m can be expressed as a linear function of $\tilde{C}_{scat,m}$ with the instrument dependent slope s and intercept c (Walser et al., 2017).

$$U_m = \tilde{C}_{scat,m} \cdot s + c \tag{3.3.3}$$

For a real OPC, the non-uniformity of the laser intensity within the sampling volume, causes blurred signal peak voltages. As a consequence, the signal peak voltages U_m must be changed to probability density functions (PDF) with a Gaussian shape and standard deviation b. Walser et al., 2017 derived the kernel function in the following way:

$$\kappa_i(D_p) = \frac{1}{\sqrt{2\pi b}} \int_0^\infty \frac{1}{U_i} \exp\left(\frac{\left(\tilde{C}_{scat,m}(D_p^{'}) - \frac{U_i - c}{s} \right)^2}{2b^2 U_i^2} \right) - \frac{1}{U_{i+1}} \exp\left(\frac{\left(\tilde{C}_{scat,m}(D_p^{'}) - \frac{U_{i+1} - c}{s} \right)^2}{2b^2 U_{i+1}^2} \right) dD_p' \tag{3.3.4}$$

The parameter b is like c and s an instrument-specific one and characterizes the signal broadening of the OPC. In Walser (2017) the signal broadening of the SkyOPC was derived with b = 0.3. This value was used for the parameter b in this thesis work.

Fig. 3.3.1 shows an example of kernel functions of the SkyOPC. The kernel functions are giving the probabilities for particle diameters to be sorted into the predefined OPC bins according to their scattering voltage signal. The different bins are visualized with colours. The black line represents the theoretical scattering cross section $\tilde{C}_{scat,m}$ of polystyrene latex particles with a spherical shape and refractive index of 1.585.

The task of calibrating the instrument is to determine the parameters c and s of the linear correlation between the scattering cross section and the signal peak voltages. With the information of diameter and intrinsic properties (refractive index etc.) of the particles, these can be determined. Polystyrene latex (PSL) particles are appropriate for this. The particles are suspended in pure water, have a defined size and are of spherical shape. For the calibration of OPC1 and OPC2 PSL particles with a diameter of 303, 400, 600, 903 and 1361 nm were used. The associated scattering cross section was calculated for a refractive index of 1.586.

The calibration measurements were carried out on the 22nd of April during the A-LIFE field campaign. For c and s, a set of values were calculated with the Markov chain Monte Carlo (MCMC) method.

The results of the calibration of OPC1 and OPC2 are depicted in the Appendix. A detailed description of the calibration process can be found in Walser et al., 2017.

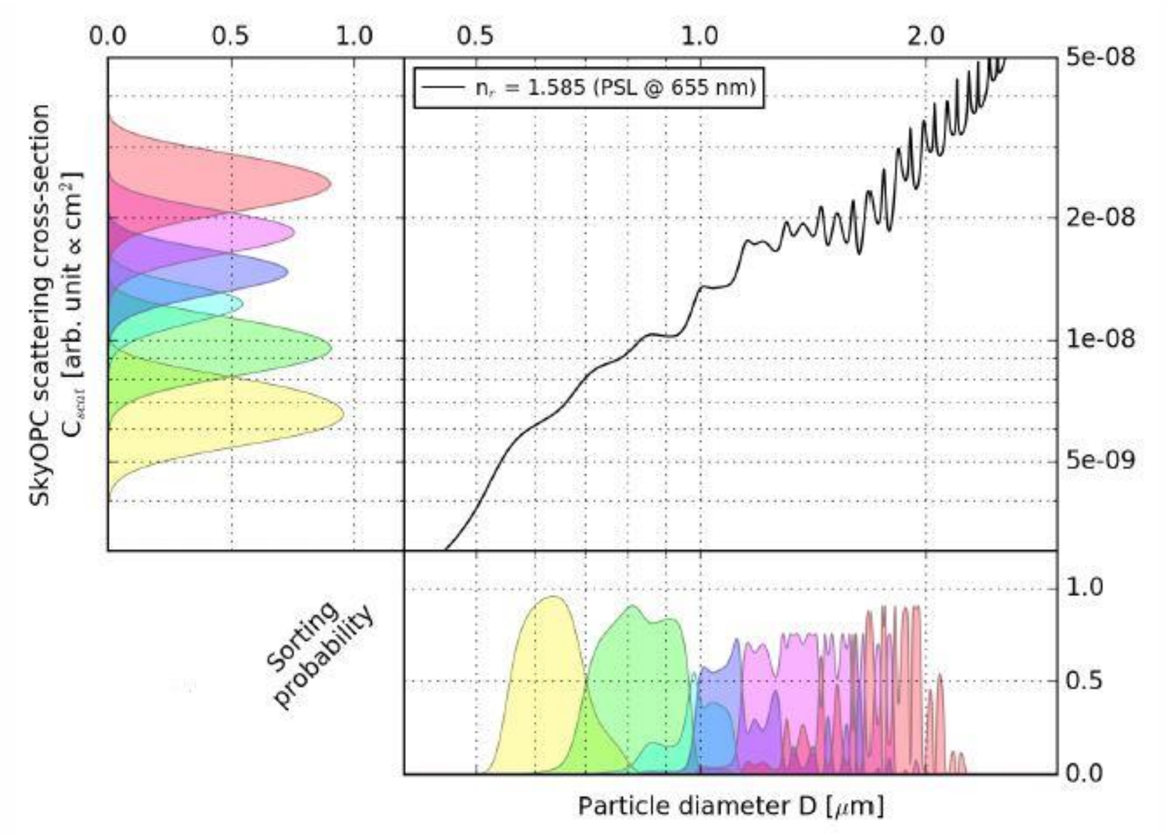

Figure 3.3.1: Sorting probability for the scattering cross section and its corresponding particle diameter for the different bins of the SkyOPC. The bins are visualized by different colours. The black line represents the theoretical particle cross section of spherical particles with a refractive index of 1.585 and an incident light with a wavelength of 655 nm. Figure adopted from Walser et al., 2017.

Starting from the resulting parameter ensembles the NSD solutions are derived with the Monte Carlo method. Thereby the parameters were drawn randomly from the whole ensemble. In addition, a set of particle cross section for different refractive indices were considered. For a range from 1.5 to 1.6 for the real part and from 0 to 0.005 for the complex part, the particle cross sections were picked randomly. Furthermore, the values of $\tilde{C}_{scat,m}$ were multiplied with a factor ϵ, characterizing the possible uncertainties of the theoretical calculation. All this values were used for the calculation of the kernel function.

The inverse problem of Eq. 3.3.2 can be avoided by calculating the so-called "perfect" mean diameter $D_{p,i}$ and widths W_i with the kernel functions (Rosenberg et al., 2012).

$$W_i = \int_0^\infty \kappa_i(D_p)\, dD_p \qquad (3.3.5)$$

$$D_{p,i} = W_i^{-1} \int_0^\infty D_p\, \kappa_i(D_p)\, dD_p \qquad (3.3.6)$$

The number size distribution $n(D_{p,i})$ for the i-th bin is now given by

$$n(D_{p,i}) = W_i^{-1} N_i \qquad (3.3.7)$$

3.3.3 Instrumental setup required for the inlet characterizations

For the characterization of the different inlets, size distributions of several instruments were compared. The sampling from different inlets give an information of the size-dependent loss in these inlets. The size distributions were measured by two instruments. One instrument was connected to a certain inlet and the other one acted as a reference instrument. Therefore, the following equation was used.

$$\eta(D_p) = \frac{n(D_p)}{n_{ref}(D_p)} \qquad (3.3.8)$$

η is the efficiency for a certain particle diameter D_p, n the number concentration of aerosol particles with this diameter measured behind a certain inlet and n_{ref} the reference number concentration.

During the flights it was possible to switch OPC2 away to different inlets besides the isokinetic inlet. The setup of the instrument and sampling lines allowed a connection to the sideward inlet. Furthermore, OPC2 was temporarily used as a reference instrument detecting the aerosol size distribution in the sampling line of the Cloud Condensation Nuclei Counter (CCNC) behind the CPS. This means OPC2 measured behind the orifices used to keep the pressure in the CPS constant. In connection with data from OPC1 it allowed to characterize particle losses in the orifices. The isokinetic and sideward inlet were characterized by comparing data of OPC1 and OPC2 with the wing-mounted CAS which is not (respectively minimally) affected by particle loss.

For comparison of the measurements of the two OPCs, it is important that they have the same size-dependent counting efficiency. Even though the instruments are identical, this can’t be considered as given, but by comparing OPC1 and OPC2 data during periods in which both instruments were sampling from the isokinetic inlet and the thermodenuder was off, a correction can be derived.

The flight sequences in which the thermodenuder was turned off, OPC2 was connected to the sideward inlet respectively on the CCNC inlet are summarized in Tab. 3.1 and 3.2. The tables include the times, altitude and ambient pressure and which orifice was in use in the CCNC inlet. Only flight sequences with constant altitude and direction were considered.

For the comparison of the counting efficiencies of the SkyOPCs, a sequence from flight 20170328a (10:10:49-10:11:52 UTC) was used (see Tab. 3.1). Even though the thermodenuder was not used during this time period, the aerosol has to be transported through sampling tubes before reaching OPC1 and OPC2, respectively. The sampling tube has a spherical cross-section with a diameter of 4.57 mm and a total length of 1.54 m. The loss factor of aerosol particles through the thermodenuder was calculated with the PLC (von der Weiden et al., 2009) and the resulting transmission efficiency is depicted in the Appendix.

In the important size range of 300 nm up to 1 µm for the cutoff-diameters of the sideward inlet and the transmission efficiencies of the orifices the loss factor was determined to be negligible. Fig. 3.3.2 shows the detected size distribution of both SkyOPC of this sequence.

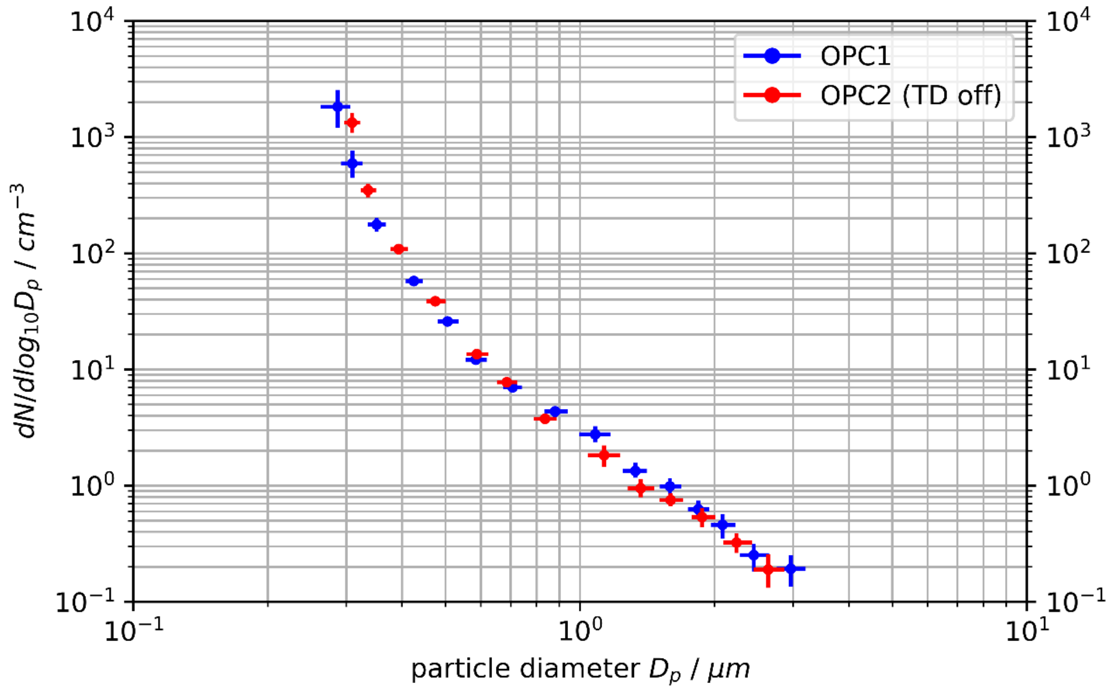

Figure 3.3.2: Size distribution from flight 20170328a (10:10:49-10:11:52 UTC) of OPC1 (blue markers) and OPC2 (red markers). During this sequence the thermodenuder before OPC2 was off.

To correct the remaining size-dependent differences in counting efficiency, factors for the first 13 size bins of OPC2 were determined. For those correction factors, the OPC1 measurements were interpolated and compared to the OPC2 measurements of the same particle size order. The ratio of the concentrations are utilized as the correction factors. The correction factors are summarized in Tab A.3 in the Appendix.

In Fig. 3.3.3 the same size distribution as in Fig. 3.3.2 is represented. The OPC2 measurements were corrected with the previous calculated factors. The result shows a smooth size distribution and good agreement of OPC1 and OPC2. The OPC2 number size distribution fits now perfectly to the one measured by OPC1. The derived correction factors were applied in all intercomparisons of data from OPC1 and OPC2 including the characterization of the sideward inlet and the CCNC inlet.

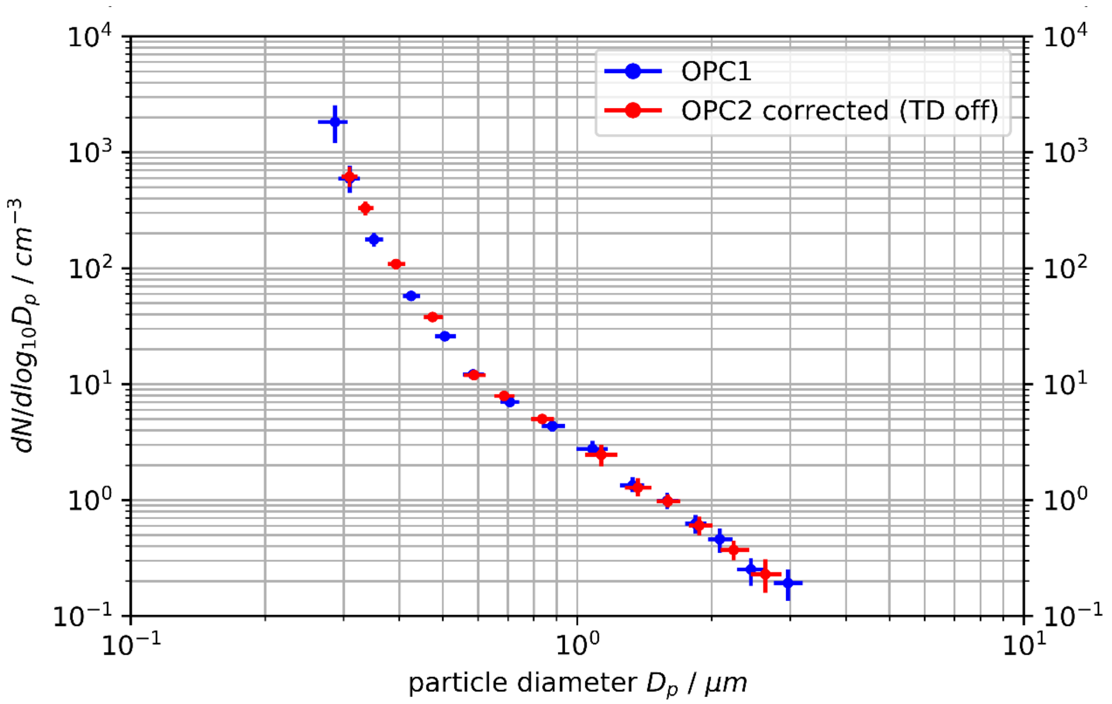

Figure 3.3.3: Size distribution from flight 20170328a (10:10:49-10:11:52 UTC) of OPC1 (blue markers) and OPC2 (red markers). The OPC2 measurements were corrected to the OPC1 measurements.

Table 3.1: Flight sequences in which the Thermodenuder was switched off and the OPC2 was connected to the sideward inlet. The tables includes values for altitude and ambient pressure. Begin and end times are in the time format hh:mm:ss UTC.

Flight	Begin	End	Altitude [m]	Ambient Pressure [hPa]
Thermodenuder off				
20170328a	09:35:24	09:43:38	10970	227
	10:01:17	10:02:57	3660	645
	10:10:49	10:11:52	780	923
OPC2 on sideward inlet				
20170328a	10:42:49	10:44:25	10670	238
	10:47:13	10:58:06	9450	288
	10:58:30	11:07:51	9450	288
	11:12:37	11:18:17	7620	376
	11:25:47	11:27:03	4880	550
	11:29:21	11:31:02	4570	572
	11:31:14	11:35:53	4570	572
	11:37:28	11:41:21	4570	572
	11:49:30	11:51:44	1430	853
20170419b	15:17:09	15:19:39	2180	783
	15:39:10	15:42:40	4690	572
	15:53:50	15:56:48	5630	506
20170422a	08:45:50	08:48:35	1270	874
	08:50:36	08:53:08	620	942
20170429b	14:01:23	14:15:44	10430	250
	14:16:06	14:21:12	10340	250

Table 3.2: Flight sequences in which the OPC2 was connected to the CCNC inlet. The table includes values for altitude, ambient pressure and specifies which orifice was used in the flight sequence. Begin and end times are in the time format hh:mm:ss UTC.

Flight	Begin	End	Altitude [m]	Ambient Pressure [hPa]	Orifice
OPC2 on CCNC inlet					
20170422a	06:49:00	06:52:45	8810	330	large
20170429a	07:10:05	07:15:00	1580	845	small
	07:16:59	07:18:38	1580	845	small
	07:18:39	07:23:36	1580	845	large
	07:24:05	07:28:54	1580	845	large
	07:29:23	07:35:09	1580	845	large
	07:50:30	08:13:24	8780	330	large
	08:31:18	08:35:21	6620	447	large
	08:36:45	08:42:01	6000	486	large
	08:44:05	08:46:57	5060	550	large
	08:48:01	08:59:39	5050	550	large
	09:01:24	09:11:12	5050	550	large
	09:11:49	09:20:29	5050	550	large
	09:24:02	09:36:54	4110	621	large
	09:37:57	09:47:56	4110	621	large
	09:49:34	09:57:45	4110	621	large
	09:58:21	10:03:52	4110	621	large
	10:06:38	10:07:45	2840	726	large
	10:08:06	10:12:06	2840	726	large
	10:13:34	10:16:00	2200	784	large
	10:16:48	10:18:55	1890	814	large
	10:18:56	10:19:06	1890	814	small
	10:21:22	10:27:44	1890	814	small
20170429b	13:08:00	13:57:23	10430	250	large

Chapter 4

Results

In this chapter the results of this thesis are presented. At the beginning the result of the characterization of the isokinetic inlet is given, followed by those of the sideward inlet. The chapter closes with the results of the characterization of the CCNC inlet.

4.1 Isokinetic inlet

For the characterization of the isokinetic inlet, the size distribution of 8 flight sequences measured by OPC1 and CAS were used. Applying Eq. 3.3.8 the particle diameter at which the counting efficiency drops to 50% was determined. The measured size distribution of CAS was used as the reference number size distribution. From the 8 available flight sequences cutoff-diameters for 5 time periods were derived. Begin and end times, altitude and ambient pressure of these 5 time periods are listed in the Appendix (Tab. A.4). The cutoff-diameters could be investigated for an altitude up to 5650 m. During the remaining 3 time periods the Falcon measured above that height and the measured concentration of particles larger than 1 µm were too low for a proper comparison between both instruments. In Tab. 4.1, the cutoff-diameters and the flight sequence-specific parameters such as pressure, temperature and TAS are listed. With those parameters the Stokes number was calculated by using Eq. 2.1.2, 2.1.4, 2.1.5 and 2.1.9. In Eq. 2.1.9 the TAS was used for V_0. For the characteristic length L, the inner diameter of the inlet was used. The inner diameter of the aerosol inlets of the Falcon is 4.572 mm. The particle density ρ_p was assumed to be 2500 kg/m^3 for mineral dust (see Kaaden et al., 2017). The result of the Stokes number and other relevant parameters are also listed in Tab. 4.1. On average, a Stokes number of $Stk_{50,iso} = (0.96 \pm 0.37)$ for the isokinetic inlet is the result.

By using $Stk_{50,iso}$ and different altitude-specific values (ambient pressure and temperature and TAS) the cutoff-diameters were calculated numerically by transforming Eq. 2.1.9 for an altitude range of 500 m up to 9500 m. These values were derived by fitting the ambient pressure and temperature and TAS, measured during the whole A-LIFE field experiment. The used fits are shown in the Appendix. Fig. 4.1.1 shows the resulting values for an altitude of up to 9500 m for three different particle densities. Fig. 4.1.1 also includes the measured cutoff-diameters. As the relaxation time of an aerosol particle, and so the Stokes number, depends on their density, the cutoff-diameters were calculated for three different values of density. The particle density ρ_p of 2500 kg/m^3 was assumed for mineral dust, 1800 kg/m^3 for ammonium sulfate. In addition, 2000 kg/m^3 was also assumed. The yellow points represents the measured cutoff-diameters and the black line in this figure the calculated altitude-dependent cutoff-diameters for the isokinetic inlet from Fiebig (2001). The used particle density for this calculation is unknown.

At an altitude of 500 m, the cutoff-diameter is between ~2.2 µm and ~2.6 µm. The diameter at which 50% of the particles passed the inlet during the A-LIFE field experiment at an altitude of 9500 m is between ~1.4 µm and ~1.7 µm. As the measured cutoff-diameters spread over a wide range (yellow dots in Fig. 4.1.1) the uncertainty of Stk_{50} is not small. Therefore, the extrapolated data from an altitude of 6000 m and upwards should just give an idea of the values of the cutoff-diameters and could have a big uncertainty.

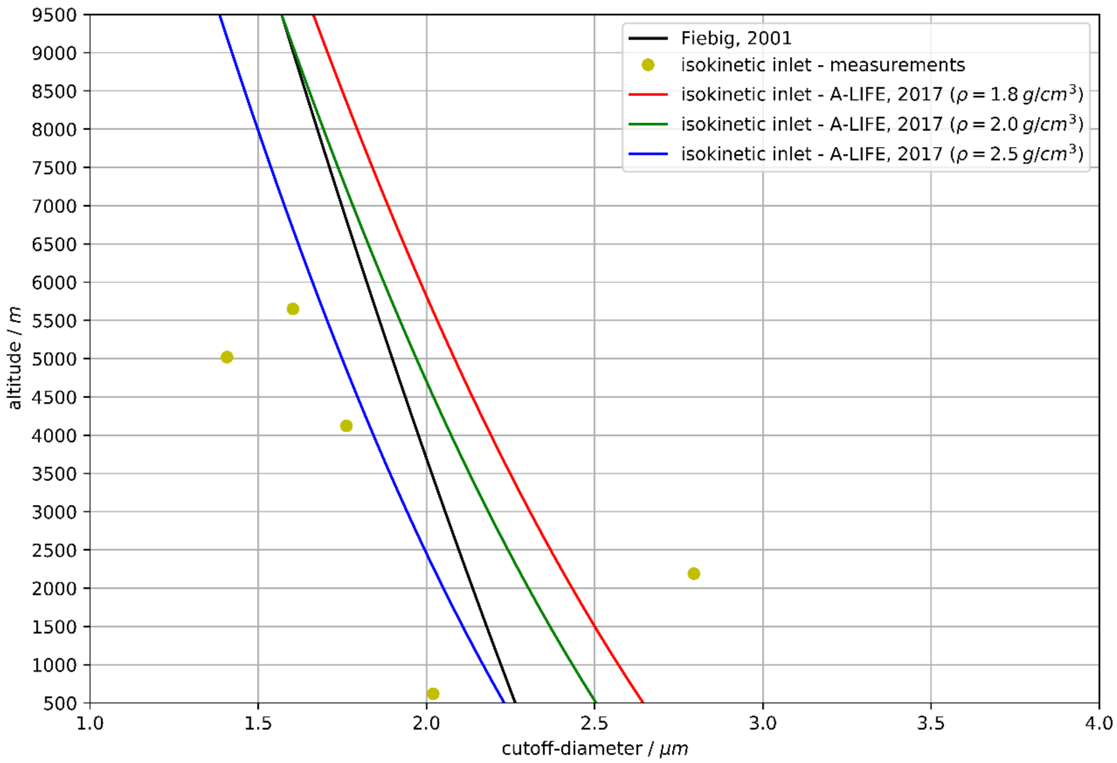

Figure 4.1.1: The cutoff-diameters of the isokinetic inlet of the Falcon for different altitudes. The red, green and blue line represents the results for different particle densities during the A-LIFE field experiment and the yellow points the measured cutoff-diameters. The black line is adopted from Fiebig (2001). Note: The CAS data used in this plot are preliminary. Results may slightly change when using the final version of the CAS data.

Table 4.1: Parameters necessary for the calculation of the Stokes number of the isokinetic inlet and the sideward inlet.

Altitude [m]	Pressure [hPa]	Temperature [K]	cutoff-diameter [µm]	dynamic viscosity [kg/ms]	TAS [m/s]	mean free path [µm]	cunningham correction [-]	Stk [-]
Isokinetic inlet								
4120	620.09	271.47	1.762	$1.71 \cdot 10^{-5}$	128	0.096	1.14	0.800
620	944.92	296.60	2.020	$1.83 \cdot 10^{-5}$	108	0.071	1.09	0.790
5020	549.82	262.52	1.407	$1.67 \cdot 10^{-5}$	140	0.100	1.19	0.600
2190	783.94	281.90	2.795	$1.76 \cdot 10^{-5}$	115	0.080	1.07	1.670
5650	507.19	258.16	1.603	$1.64 \cdot 10^{-5}$	171	0.110	1.17	0.960
Sideward inlet								
4880	549.68	258.56	0.307	$1.65 \cdot 10^{-5}$	145	0.100	1.89	0.048
4570	572.23	261.26	0.313	$1.66 \cdot 10^{-5}$	142	0.099	1.84	0.047
4570	572.40	261.35	0.315	$1.66 \cdot 10^{-5}$	146	0.099	1.84	0.049
4570	572.42	261.37	0.309	$1.66 \cdot 10^{-5}$	146	0.099	1.86	0.047
1430	853.20	280.07	0.397	$1.75 \cdot 10^{-5}$	111	0.073	1.47	0.045
2180	783.16	281.39	0.340	$1.76 \cdot 10^{-5}$	139	0.080	1.61	0.045
4690	572.40	264.46	0.325	$1.68 \cdot 10^{-5}$	136	0.100	1.82	0.047
5630	506.40	257.59	0.244	$1.64 \cdot 10^{-5}$	138	0.110	2.24	0.034
1270	874.39	295.51	0.404	$1.83 \cdot 10^{-5}$	126	0.076	1.48	0.051
620	941.40	299.35	0.412	$1.85 \cdot 10^{-5}$	125	0.072	1.45	0.051
2740	725.15	267.07	0.307	$1.69 \cdot 10^{-5}$	131	0.081	1.69	0.038

4.2 Sideward inlet

For the characterization of the sideward inlet of the Falcon, the size distribution measured by OPC1 and OPC2 were compared. The 16 sequences in which OPC2 was connected to the sideward inlet are listed in Tab. 3.1. Out of those sequences 11 cutoff-diameters up to an altitude of 5630 m could be investigated. For higher altitudes the cutoff-diameter of the sideward inlet is too small (D_p < 300 nm) and can't be detected from the SkyOPCs anymore.

All calculations were performed analogical to those for the isokinetic inlet. The cutoff-diameters, the Stokes numbers and all associated parameters are included in Tab. 4.1. For the sideward inlet, a Stokes number of $Stk_{50,side} = (4.55 \pm 0.49) \cdot 10^{-2}$ on average results.

Like for the isokinetic inlet, this Stokes number was used for a numerical calculation of the cutoff-diameters as a function of altitude. Fig. 4.2.1 shows the result of the calculation. It also includes the measured cutoff-diameters and the previously presented calculations for the isokinetic inlet and the findings from Fiebig (2001) for the backward inlet. This inlet was not used during the A-LIFE field experiment.

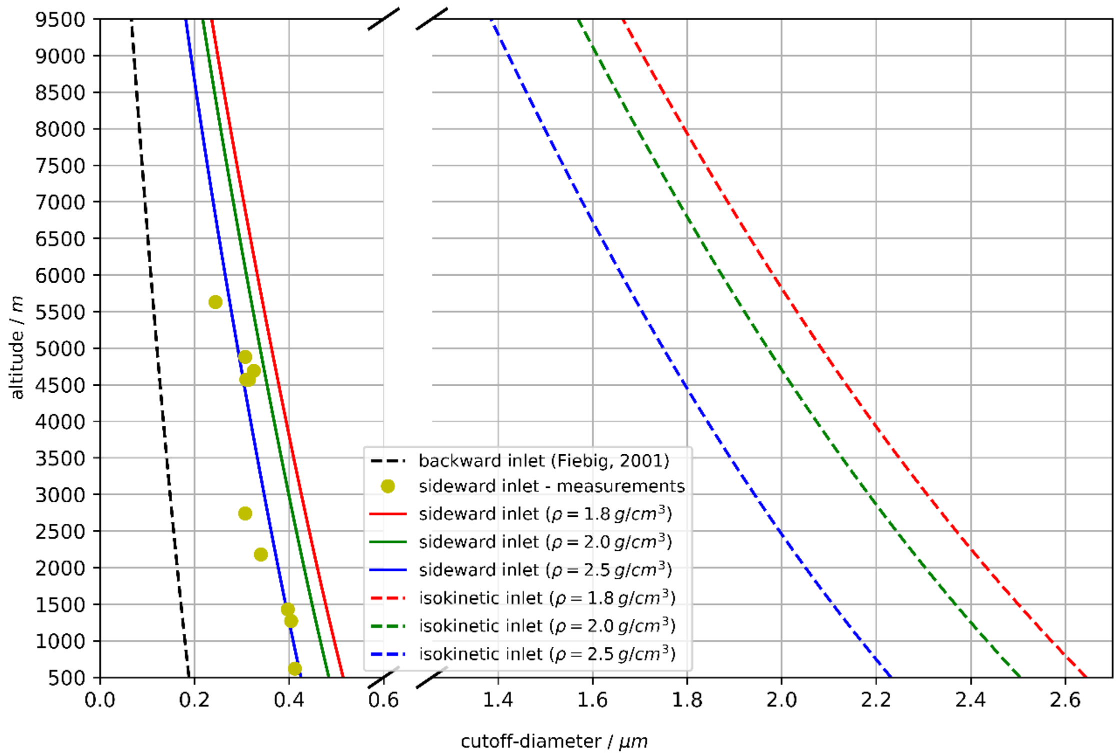

Figure 4.2.1: The cutoff-diameters of the sideward inlet of the Falcon for different altitudes. The red, green and blue line represents the results for different particle densities during the A-LIFE field experiment and the yellow points the measured cutoff-diameters. The black dashed-line is adopted from Fiebig (2001) and represents the cutoff-diameter for the backward inlet, which was not in use during the A-LIFE field experiment. In this figure also the previous results for the isokinetic inlet are included on the right side.

At an altitude of 500 m, the cutoff-diameter of the sideward inlet is between ~400 nm and ~500 nm. The diameter at which 50% of the particles passed the sideward inlet at an altitude of 9500 m is between ~200 nm and ~250 nm. As for the isokinetic inlet, the cutoff-diameters in Fig. 4.2.1 for the sideward inlet are extrapolated up to an altitude of 9500 m. This values should only give an idea of the cutoff-diameters and could comprise an uncertainty.

For a better understanding of the efficiency of the sideward inlet, its size-dependent transmission efficiency grouped for different ambient pressures, respectively altitudes, was calculated. Decreasing ambient pressure leads to decreasing transmission efficiency. On a higher altitude, meaning lower ambient pressure, the research aircraft has to fly faster. As a consequence, it is harder for the particles to follow the streamlines into the sideward inlet. This effect can be seen in Fig. 4.2.2. In this figure the inlet efficiency is shown for three different ambient pressure ranges.

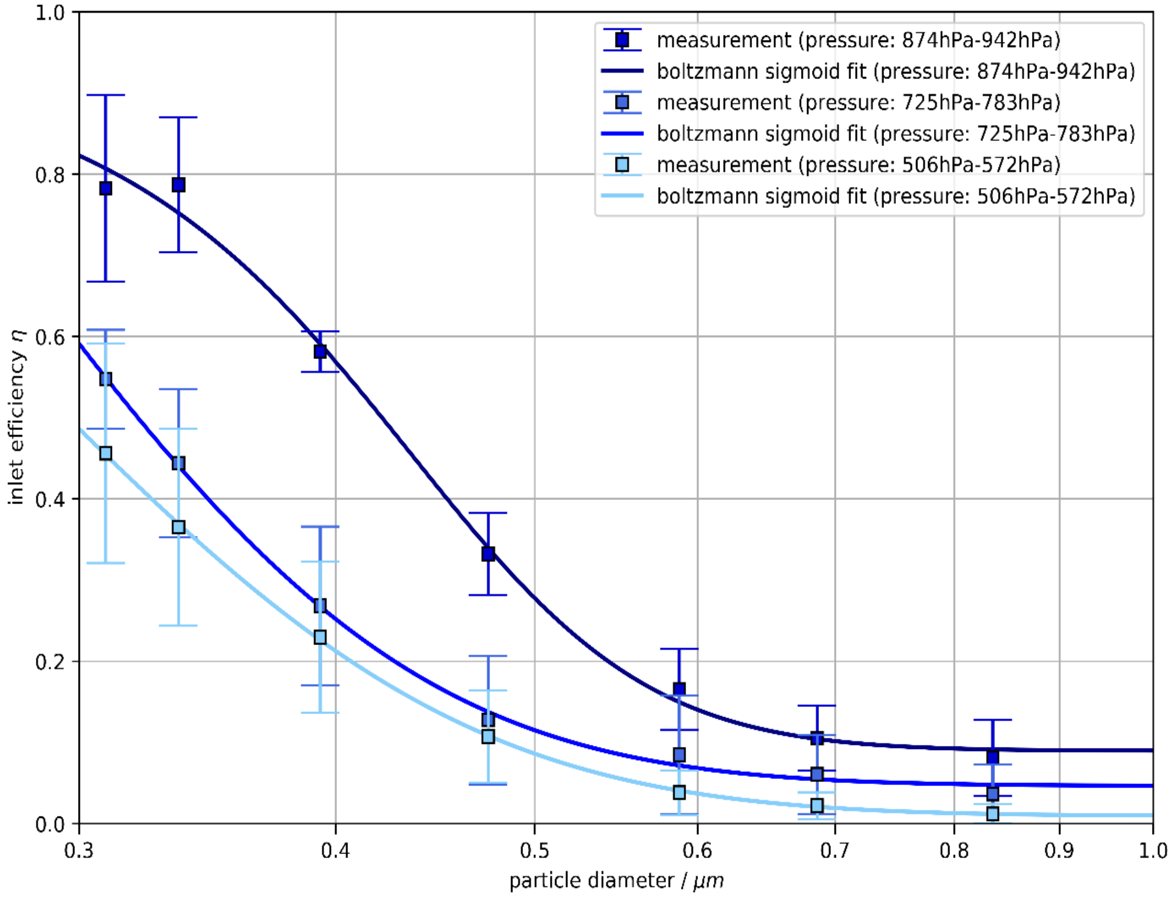

Figure 4.2.2: Inlet efficiency of the sideward inlet for different ambient pressure ranges. Fitted with a Boltzmann sigmoid function.

The first range of the ambient pressure (874 hPa-942 hPa) corresponds to an altitude of 620 up to 1430 m. An ambient pressure of 725 hPa to 783 hPa covers an altitude of the research aircraft of 2180 to 2730 m, the last pressure-range (506 hPa-572 hPa) of 4570 to 5630 m. The measurements are fitted with a Boltzmann sigmoid function (Eq. 4.2.1). The fit parameters (h, k and x_0) are listed in the Appendix (Tab. A.5).

$$y = \frac{(1-h)}{1+\exp\left(\frac{(x_0-x)}{k}\right)} + h \tag{4.2.1}$$

4.3 CCNC inlet

The aim for the CCNC inlet was to investigate the transmission efficiency of the two orifices used for the CPS. As seen in Tab. 3.1, OPC2 was connected to the CCNC sampling line during 4 sequences, when the small aperture orifice was used, and 20 sequences, when the large aperture orifice was used. The transmission efficiency was calculated with Eq. 3.3.8 with the measured size distribution of OPC1 as the reference.

For the transmission efficiency of the small aperture orifice 3 out of the 4 sequences were used and the mean and standard deviation were calculated. The fourth sequence from flight 20170429a (10:21:22-10:27:44 UTC) was not considered. In this sequence the OPC2 measured a much higher number size distribution than OPC1. This is unphysically because of the high particle loss in the small aperture orifice. Fig. 4.3.1 shows the transmission efficiency of both orifices. The measurements are fitted with a Boltzmann sigmoid fit (Eq. 4.2.1) for a particle size range from about 250 nm up to 1 µm. The fit parameters are given in the Appendix. The transmission efficiency is at 75% at a particle size of around 300 nm. It drops to about 30% for particle diameters of about 650 nm. The diameter at which 50% of the particles pass the orifice is about 460 nm. The violet measurement points in Fig. 4.3.1 are the mean of the 3 sequences and the error bars correspond to the standard deviation of the mean.

The same as for the small aperture orifice has been done for the large aperture orifice. For the calculation of the mean and standard deviation only the flight sequences up to an ambient pressure of 500 hPa were considered. 80% of the particles pass the orifice at a particle diameter of about 330 nm. The cutoff-diameter of the large orifice is with about 480 nm a little bit larger to the one of the small aperture orifice. Towards larger particles the transmission efficiency decreases to ~27%. The orange measurement points in

Fig. 4.3.1 are the mean of the 15 sequences and the error bars were calculated with the standard deviation of the mean.

Dollner (2015) determined the transmission efficiency for the large aperture orifice with PSL particles for an inlet pressure of about 930 hPa. These measurements were carried out in the laboratory. PSL particles have a density of 1100 kg/m^3. For a better comparability to aircraft measurements, Walser (2017) converted these measurements to spherical particles with a density between 1600 kg/m^3 and 2600 kg/m^3. This range includes the particle densities of 1800 kg/m^3 (ammonium sulfate) and 2500 kg/m^3 (mineral dust).

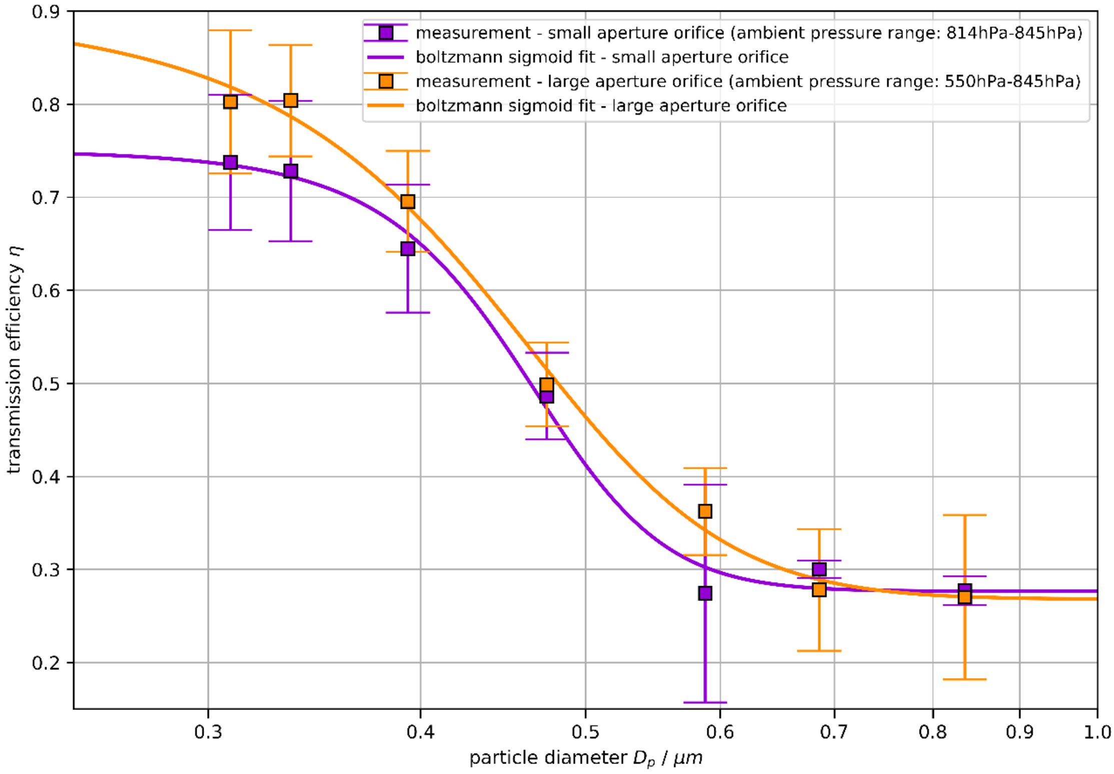

Figure 4.3.1: Transmission efficiency of the small aperture orifice and large aperture orifice used for the CPS of the CCNC during the A-LIFE field experiment.

The transmission efficiency shifts to lower values. To compare the measurements of Dollner (2015) and the conversion of Walser (2017) the transmission efficiency of the flight sequences with the lowest altitude were considered. As the pressure difference plays a role for the transmission efficiency, the measurement with the highest ambient pressure is the closest to the measurement of Dollner (2015) with laboratory conditions. These are the 3 flight sequences at an altitude of 1580 m and an ambient pressure of 845 hPa.

The result is depicted in Fig. 4.3.2. The orange markers and line represent the laboratory measurements with PSL particles. The dashed lines are the converted function of the laboratory measurement for spherical particles. In black, the points represent the aircraft measurement at 845 hPa. These data points are fitted with a Boltzmann sigmoid function. The transmission efficiency of the large aperture orifice calculated in this thesis work for the A-LIFE field experiment are in good agreement with the converted functions up to a particle diameter of 400 nm. For larger particle diameters the transmission efficiency is lower than the converted functions. These deviations are, however not significant compared to the uncertainties of the calculated transmission efficiency.

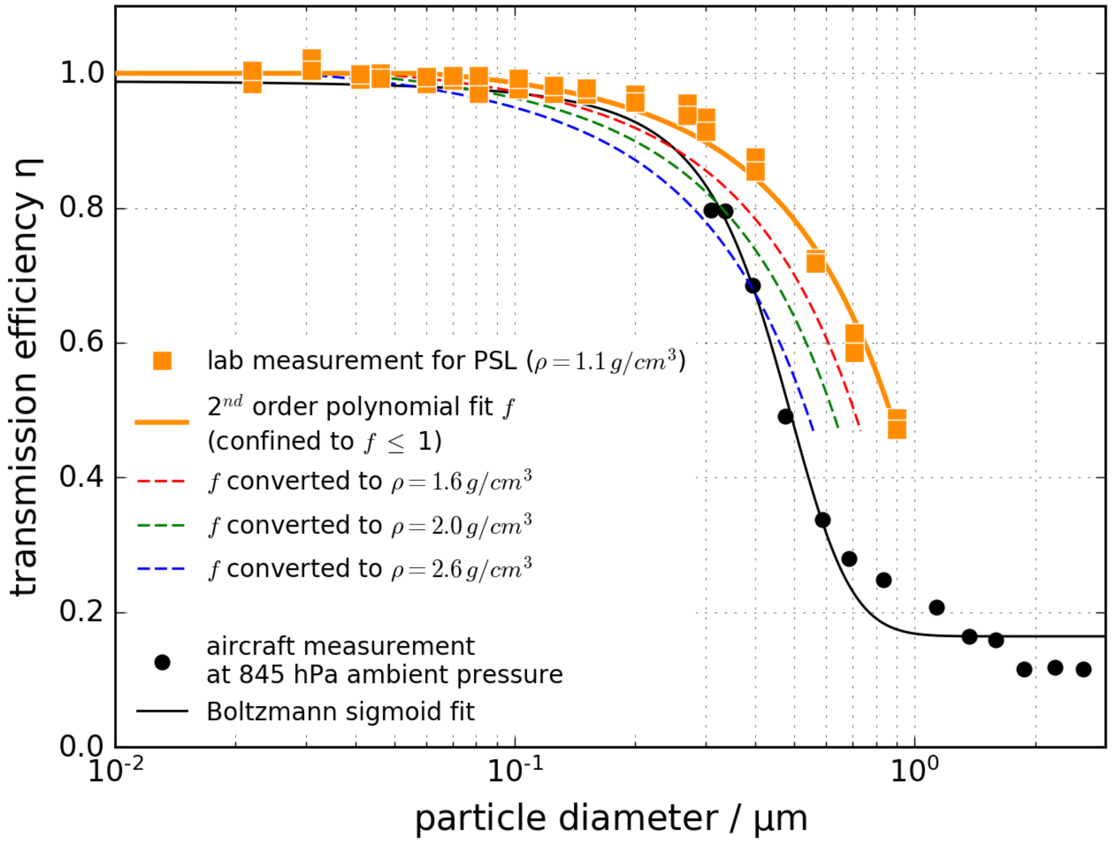

Figure 4.3.2: Transmission efficiency of the large aperture orifice. The orange markers and line represents the laboratory measurements from Dollner (2015). The dashed lines show the converted functions of the laboratory measurements from Walser (2017). The black points are the measurements observed during the A-LIFE field experiment at an ambient pressure of 845 hPa. These data pints were fitted with a Boltzmann sigmoid function. This figure was provided by Adrian Walser.

Chapter 5

Discussion

As already mentioned in the previous chapter, the characterization for the isokinetic inlet of the Falcon has been done analogical to Fiebig (2001). In this PhD thesis, the cutoff-diameters were measured up to an altitude of 2 km. Overall, the cutoff-diameters are slightly larger than those investigated during the A-LIFE field experiment. This means that there was a better inlet efficiency during the Lindenberger Aerosol Charakterisierungsexperiments (LACE) field campaign in 1998. One reason for this could be the flow velocity. As discussed in chapter 2, the best condition for a high sampling efficiency is given when the flow velocity of the free-stream gas equals the flow velocity after the inlet. This condition is indicated as isokinetic sampling. The speed of the research aircraft is roughly between 100 and 190 m/s. For the best sampling efficiency, a high flow velocity after the inlet, close to the velocity of the ambient air, is required. During the LACE field campaign, the flow velocity after the isokinetic inlet was 27.3 m/s. In contrast to the flow velocity of 18.67 m/s during the A-LIFE field experiment. This velocity can change because of the different instrumental setup and the different sampling volume needed by these instruments. In both campaigns the Stokes number for the isokinetic inlet calculated with the cutoff-diameters are overall smaller than 1. The curves in Fig. 2.2.3 for Stokes numbers smaller than 1 verifies the better inlet efficiency, as the flow velocity during the measuring campaign in 1998 was higher compared to the A-LIFE project.

Of course, the deviations in cutoff-diameters lead to a different Stokes number. Beside the fact that the Stokes number depends on the ambient temperature and pressure, which can vary from day to day and from location to location. The Stokes number of the isokinetic inlet during the A-LIFE field experiment is higher but within the same order of magnitude as in the LACE campaign. As for the numerical calculation of the cutoff-diameters as a function of altitude, the Stokes number was held constant. This leads to a deviation of the calculated cutoff-diameters between the two campaigns (see Fig. 4.1.1).

For this thesis, the cutoff-diameter were calculated for the isokinetic inlet with three different values for the particle density. Those investigated by Fiebig (2001) lies between the curves for particles with a density of 2500 kg/m^3 and 2000 kg/m^3. The used particle density is not quoted in Fiebig (2001) and could not be recalculated with the given parameters.

The characterization of the sideward inlet of the Falcon has been done systematically for the first time. For this thesis work, the cutoff-diameter and the Stokes number were calculated in the same way as for the isokinetic inlet. As expected, the values of the sideward inlet are larger than the values of the backward inlet calculated by Fiebig (2001). As for the isokinetic inlet, the cutoff-diameters were also recalculated for three different particle densities. Depending on which aerosol species are measured, these results give an idea of how many particles would pass the inlet and were measured with an aerosol in-situ instrument in the cabin of the research aircraft.

For a more precise investigation of the cutoff-diameters of the sideward inlet and calculation of its Stokes number more instruments have to be used. Above an altitude of about 5 km the cutoff-diameters are too small to be detected by the Grimm SkyOPCs with a detection range starting from around 300 nm. Therefore, the data of other instruments should have been considered to calculate the number size distribution, including smaller particles. This was not possible during the A-LIFE field campaign as only OPC2 was switchable to the sideward inlet and no other instrument, which can detect a particle number size distribution.

The calculated transmission efficiencies of the two orifices used for the CCNC inlet system give an idea of the particle loss. The ones of the large aperture orifice are in good agreement with the recalculated efficiencies of Walser (2017) for different particle densities up to a particle diameter of about 400 nm. For larger particles the transmission efficiency is lower compared to the recalculated curves for spherical particles.

It has to be mentioned that the recalculated transmission efficiencies resulted from measurements carried out in the laboratory and the converted functions were calculated for spherical particles. Aerosol measurements with a research aircraft can’t really be compared against these curves and have to be treated with caution. The different ambient conditions can influence the aerosol measurements. Furthermore, the research aircraft measures spherical and aspherical aerosol particles.

The altitude range in which the small aperture orifice was used is not really big. The large aperture orifice was used for a larger altitude range respectively ambient pressures. Because of that the transmission efficiencies can be considered separately for different ambient pressure ranges for a more detailed look at the result. Fig. 5.1 shows the transmission efficiency of the large aperture orifice for different ambient pressures or ambient pressure ranges. The expectation of these separated efficiencies are higher values at lower ambient pressures.

As already mentioned in chapter 3, the CCNC operates at a fixed pressure of 500 hPa. The bigger the gap between ambient pressure and the operating pressure of the CCNC, the bigger is the turbulence behind the orifice, resulting in higher particle loss.

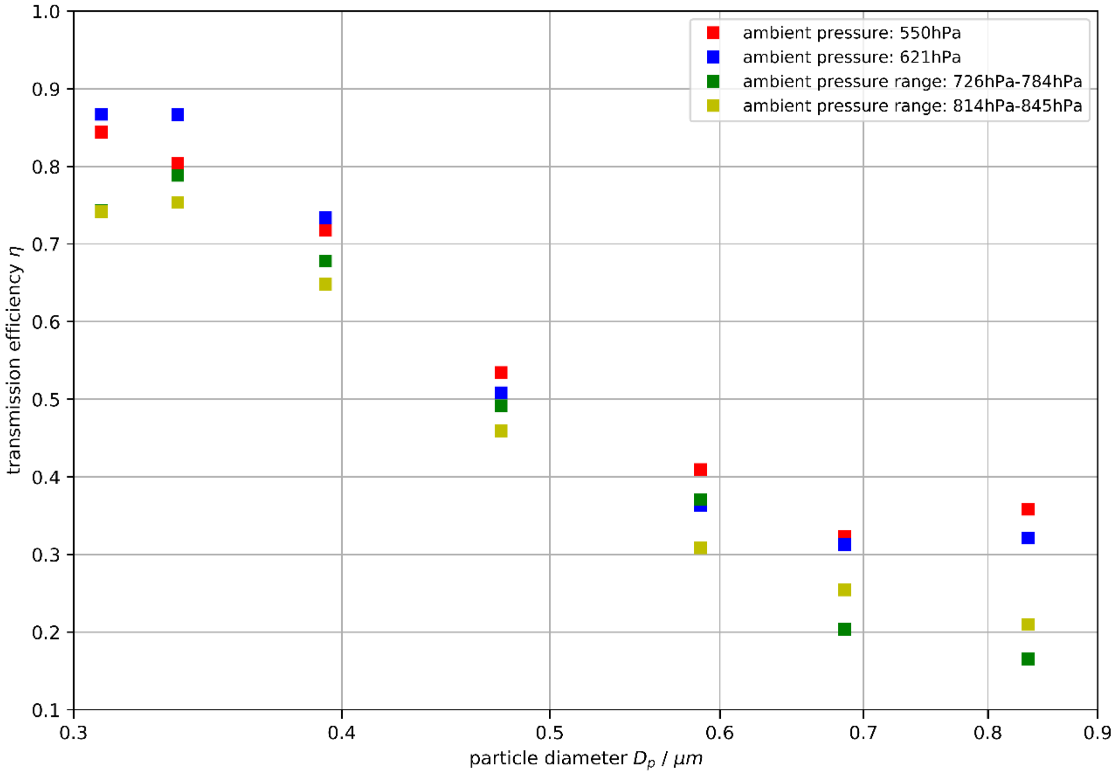

Figure 5.1: Transmission efficiency of the large aperture orifice for different ambient pressure and pressure ranges.

As seen in Fig. 5.1, this is not the case at every particle diameter. For example, the transmission efficiency at an ambient pressure of 550 hPa is smaller than at 621 hPa until a particle diameter of about 480 nm. For larger particles, the best efficiency is given for an ambient pressure of 550 hPa. It is also surprising the efficiencies are higher at an ambient pressure of about 830 hPa compared to about 750 hPa for particles with a diameter larger than 690 nm. Although these calculations have uncertainties which should be kept in mind and can potentially change the arrangement of the measurement dots in Fig. 5.1.

Different efforts were made to precise the transmission efficiency of the large aperture orifice. The first approach was made regarding the particle loss in the sampling lines inside the aircraft cabin: For the characterization of the sideward inlet the losses in the sampling lines to OPC1 and OPC2 were assumed to be the same. So for the comparison, the losses due to the transport of the aerosol particles to the instruments cancel out and the loss is only affected by the misalignment of the sideward inlet. For the CCNC inlet calculations, OPC1, connected to the isokinetic inlet, and OPC2, used as a reference instrument to the CCNC, were considered. When the OPC2 was connected to the CCNC, the sampling line from the isokinetic inlet to the instrument was long compared to the sampling line of OPC1. The long sampling line could lead to bigger particle losses. A correction of the measured concentrations by OPC2 could potentially result in a higher transmission efficiency of the large aperture orifice. Therefore, the particle loss calculator (von der Weiden et al., 2009) was used to quantify the transport efficiency of the sampling line of OPC2. The calculations with this tool were performed by Clemens Weselka, University of Vienna. The transport efficiency through the sampling lines upstream of OPC2 is worse than of OPC1 but the deviations are not significant. In the range of a particle size from 300 nm to 700 nm the difference is only between 5% and 8%. This doesn't lead to a significant difference to the previously calculated transmission efficiency of the large aperture orifice. As a consequence, sampling line losses were no longer considered.

Beside the theoretical calculation of the transport losses in the sampling line to OPC2 an "experimental" approach was made. During some flights, the CCNC operated on the ambient pressure meaning that the orifices were not used. The comparison between the measurements of OPC1 and OPC2, both connected to isokinetic inlet, gives the losses of the sampling line of OPC2. This correction would lead to a higher transmission efficiency of the large aperture orifice. The reason why this correction was not considered for the final result, was the pump of the CPS. The pump was still running during these flight sequences which implies undefined conditions in the CPS.

Chapter 6

Conclusion

In this study different aerosol inlets, which were used during the A-LIFE field experiment, were characterized. For the main inlets of the research aircraft Falcon, the isokinetic and the sideward inlet, the cutoff-diameters as a function of altitude were calculated. Furthermore, the inlet of an in-cabin instrument, the CCNC, was characterized. This inlet provides a constant pressure for the CCN measurements using a system with two different orifices in the aerosol flow. The transmission efficiency of these orifices were derived in this thesis work. All of the results were achieved by comparing size distributions measured by different instruments during the A-LIFE project.

The cutoff-diameter of the isokinetic inlet was inferred to be ~2.4 µm at lower altitudes decreasing to about 1.6 µm at an altitude of 9500 m. For particles larger than the cutoff-diameter the number concentrations can decrease rapidly due to the inlet system, leading to significant discrepancies between the observations and the (true) properties of the ambient aerosol. For this reason, it is important to know the cutoff-diameters of this inlet at different aircraft altitudes and to correct the observed number concentrations by the instruments with this thesis work.

The characterization of the sideward inlet is important for the A-LIFE project since two Tri-color Absorption Photometer (TAP) were operated at two different inlets, the isokinetic and the sideward inlet, in order to measure the absorption coefficient in two different size ranges. For the sideward inlet the cutoff-diameters were determined as a function of altitude. At an altitude of 500 m the cutoff-diameter is 450 nm, decreasing to 200 nm at an altitude of 9500 m.

Besides isokinetic and sideward inlets, also the CCNC inlet system utilizing two orifices to achieve constant pressure was characterized. The transmission efficiencies of the orifices used for the Constant Pressure System show that there are particle losses which can’t be neglected. It is shown that only 50% of the particles with a diameter of about 460 nm pass the small aperture orifice and particles with a diameter of about 480 nm the large aperture orifices. With an increasing particle diameter the transmission efficiency decreases to lower values. The calculations in this thesis will help to correct the measured concentrations of the CCNC and to get a precise outcome of this data set.

The field campaign in Cyprus was conducted about two years ago and the A-LIFE project is in the final phase of data analysis. The results of this thesis work will add another level of precision and accuracy to the final analysis of the A-LIFE project. It is clearly shown in this thesis that particle losses caused by the different inlet systems lead to a distortion of the measurements and appropriate corrections are imperative. In this thesis it is demonstrated that particle losses due to the different inlets, which were used during the A-LIFE field experiment, have to be considered in the data analysis.

Appendix A

Tables

Table A.1: List of all instruments installed on the research aircraft Falcon during A-LIFE. Extracted from the A-LIFE website www.a-life.at (Accessed: 1 February 2019).

Instrumentation	Measured quantity
Inside the DLR Falcon cabin behind an isokinetic inlet (D_p < 2.5 µm)	
Condensation Particle Counters (CPC), 3 CPCs with different lower cut-off, 1 reference CPC for CCN measurements	Total number concentration of fine mode particles (0.005 µm < D_p < 2.5 µm)
Optical Particle Counter (SkyOPC), type Grimm Sky 1.129	Total size distribution (0.25 µm < D_p < 2.5 µm)
Heated inlet CPC's and SkyOPC	Non-volatile size distribution (0.01 µm < D_p < 2.5 µm)
Envitech Optical Particle Analyzer (OPAL)	Simultaneous measurement of size distribution (~0.5 µm < D_p < 5 µm) and complex refractive index (660 and 808 nm)
Polar nephelometer	Particle light scattering coefficient at three wavelengths (450, 525, 635 nm). Light scattering coefficients will be recorded for total scattering and hemispheric backscattering.
Single Particle Soot Photometer (SP2)	Refractory black carbon mass in the range 5-104 fg, corresponding to an equivalent size range of 80-480 nm, single-particle coating thickness, mixing state
Two 3-λ-Tri-color Absorption Photometers (TAP)	Absorption coefficient of total and sub-micron aerosol at three wavelengths (467, 528, 652 nm)
Cavity Attenuated Phase Shift Single Scattering Albedo Monitor (CAPS PMssa)	Extinction and scattering coefficient (630 nm), single scattering albedo
Dual Column Cloud Condenstation Nuclei Counter (CCNC)	Number concentration of cloud condensation nuclei at various supersaturations
Impactor devices	Chemical particle composition, refractive index, shape
At DLR Falcon wing stations	
Ultra-high Sensitivity Aerosol Spectrometer – Airborne (UHSAS-A)	Aerosol size distributions (0.06 µm < D_p < 1 µm)
Passive Cavity Aerosol Spectrometer Probe (PCASP-100X)	Dry state accumulation mode (0.12 µm < D_p < 3.5 µm)
Cloud and Aerosol Spectrometer with Detector for Polarization Detection (CAS-DPOL)	Aerosol particle and cloud hydrometeor size distributions (0.5 µm < D_p < 50 µm), particle optical properties, particle shapes
Second generation Cloud, Aerosol, and Precipitation Spectrometer with Polarization Detection (CAPS)	Aerosol particle and cloud hydrometeor size distributions (0.5 µm < D_p < 930 µm), particle optical properties, particle shapes, liquid water content, aircraft velocity
Remote sensing instruments	
2-µm pulsed Doppler wind lidar	Vertically resolved horizontal wind vector (conical scan), vertical wind speed (nadir pointing), and backscatter coefficient (conical scan and nadir pointing)
Meteorological sensors	
Falcon nose boom instrumentation	Position, temperature, pressure, humidity, 3D-wind

Table A.2: List of A-LIFE research flights date, times, locations and objectives. Extracted from the A-LIFE website www.a-life.at (Accessed: 1 February 2019).

Date	Takeoff	Landing	From	To	Objective
2017/03/28	09:00:47	11:57:18	Oberpfaffenhofen (DE)	Oberpfaffenhofen (DE)	Dust sampling over France and Germany
2017/03/31	07:35:42	10:43:59	Oberpfaffenhofen (DE)	Oberpfaffenhofen (DE)	Comparison of pollution levels over two major European cities (Munich, Vienna) in comparison with the tropospheric background site Mount Sonnblick GAW Observatory
2017/04/03	06:08:30	09:01:59	Oberpfaffenhofen (DE)	Cagliari (IT)	Transfer flight, in-situ profiling over Mount Sonnblick GAW Observatory, Genoa and Sardinia (aged dust)
2017/04/03	12:38:03	15:49:47	Cagliari (IT)	Paphos (CY)	Transfer flight, dust ahead of a low pressure system; in-situ profiling near Crete
2017/04/05	08:50:01	12:08:09	Paphos (CY)	Paphos (CY)	Middle East/Arabian dust, cloud-free conditions
2017/04/06	04:30:27	08:05:57	Paphos (CY)	Paphos (CY)	Middle East/Arabian (low altitudes) & Saharan dust (higher altitudes), cloud-free conditions
2017/04/11	05:04:10	08:56:45	Paphos (CY)	Paphos (CY)	Dust in the Cyprus area before trough passage; „pattern cloud“; heavily polluted atmosphere at 2000ft over the sea south of Cyprus
2017/04/11	09:56:35	12:59:01	Paphos (CY)	Paphos (CY)	Dust in the Cyprus area before trough passage; „pattern preferred“
2017/04/13	08:27:31	11:46:42	Paphos (CY)	Paphos (CY)	Dust embedded in clouds, ice formation at high temps; heavy pollution at low altitudes over the sea south of Cyprus; polluted dust down to the ground
2017/04/14	04:07:35	07:58:23	Paphos (CY)	Heraklion (GR)	Dust and pollution sampling over Crete; in-situ profiling over Finokalia before landing; indications for vertical mixing inside the dust layer; dust gradient with dust surge east of Crete
2017/04/14	09:03:58	12:24:40	Heraklion (GR)	Paphos (CY)	Dust and pollution sampling over Crete; in-situ & lidar flight with W-E profiling Finokalia; dust gradient with dust surge east of Crete
2017/04/19	09:58:52	13:56:52	Paphos (CY)	Malta (MT)	Beginning of a Saharan dust outbreak which moved eastwards; lidar flight Cyprus - Malta with vertical in-situ profiling in the Malta region
2017/04/19	15:10:26	19:06:37	Malta (MT)	Paphos (CY)	Beginning of a Saharan dust outbreak which moved eastwards; in-situ profiling after take-off in Malta; chasing of dust-impacted clouds near Malta
2017/04/20	10:06:17	13:34:59	Paphos (CY)	Heraklion (GR)	maximum of the Saharan dust outbreak; coordinated measurements with Crete
2017/04/20	14:40:23	18:33:30	Heraklion (GR)	Paphos (CY)	maximum of the Saharan dust outbreak, chasing of dustimpacted clouds near/over Crete in the cloud top layer; aerosol-cloud interaction
2017/04/21	11:48:30	16:01:13	Paphos (CY)	Paphos (CY)	Dust sampling west and south-west of Cyprus: end of Saharan dust outbreak
2017/04/22	06:07:01	09:26:15	Paphos (CY)	Paphos (CY)	Dust sampling south of Cyprus: end of Saharan dust outbreak
2017/04/25	08:03:40	10:20:25	Paphos (CY)	Paphos (CY)	Sampling of pollution (and biomass burning?) from Turkey and the Black Sea west and north-west of Cyprus
2017/04/26	12:06:05	14:39:49	Paphos (CY)	Paphos (CY)	Arabian and Saharan dust outbreak; Saharan dust mainly in the western part of the flight pattern, Arabian dust in the south-eastern part of the flight pattern
2017/04/27	07:13:15	10:18:11	Paphos (CY)	Paphos (CY)	Arabian and Saharan dust outbreak; probably boundary of Arabian dust between Paphos and Limassol during take-off
2017/04/29	07:06:29	10:34:11	Paphos (CY)	Heraklion (GR)	Transfer flight; Saharan dust outbreak, coordinated measurements with Crete
2017/04/29	11:42:25	14:48:26	Heraklion (GR)	Oberpfaffenhofen (DE)	Flight on the back side of a low pressure system

Table A.3: Correction factors for the first 13 SkyOPC size bins.

SkyOPC bin	**correction factor [-]**
1	2.17
2	1.06
3	1.00
4	1.02
5	1.13
6	0.98
7	0.75
8	0.74
9	0.74
10	0.77
11	0.89
12	0.87
13	0.83

Table A.4: Fit parameters for the different calculated efficiencies.

Flight	Begin	End	Altitude [m]	Ambient Pressure [hPa]
20170421a	14:43:51	14:49:01	4120	620
20170421a	15:02:03	15:07:52	620	945
20170427a	07:54:28	08:04:27	5020	550
20170427a	07:28:01	07:37:59	2190	784
20170426a	12:46:50	12:48:30	5650	507

Table A.5: Fit parameters for the different calculated efficiencies.

Fig. 4.2.2: Inlet efficiency – sideward inlet (Boltzmann sigmoid fit, Eq. 4.2.1)		
874 hPa – 942 hPa	725 hPa – 783 hPa	506 hPa – 572 hPa
x_0 = 0.414	x_0 = 0.207	x_0 = 0.212
k = -0.067	k = -0.086	k = -0.094
h = 0.090	h = 0.047	h = 0.009

Fig. 4.3.1: Transmission efficiency – small aperture orifice (Boltzmann sigmoid fit, Eq. 4.2.1)

x_0 = 0.459
k = -0.045
h = 0.277

Fig. 4.3.1: Transmission efficiency – large aperture orifice (Boltzmann sigmoid fit, Eq. 4.2.1)

x_0 = 0.441
k = -0.072
h = 0.268

Appendix B

Plots

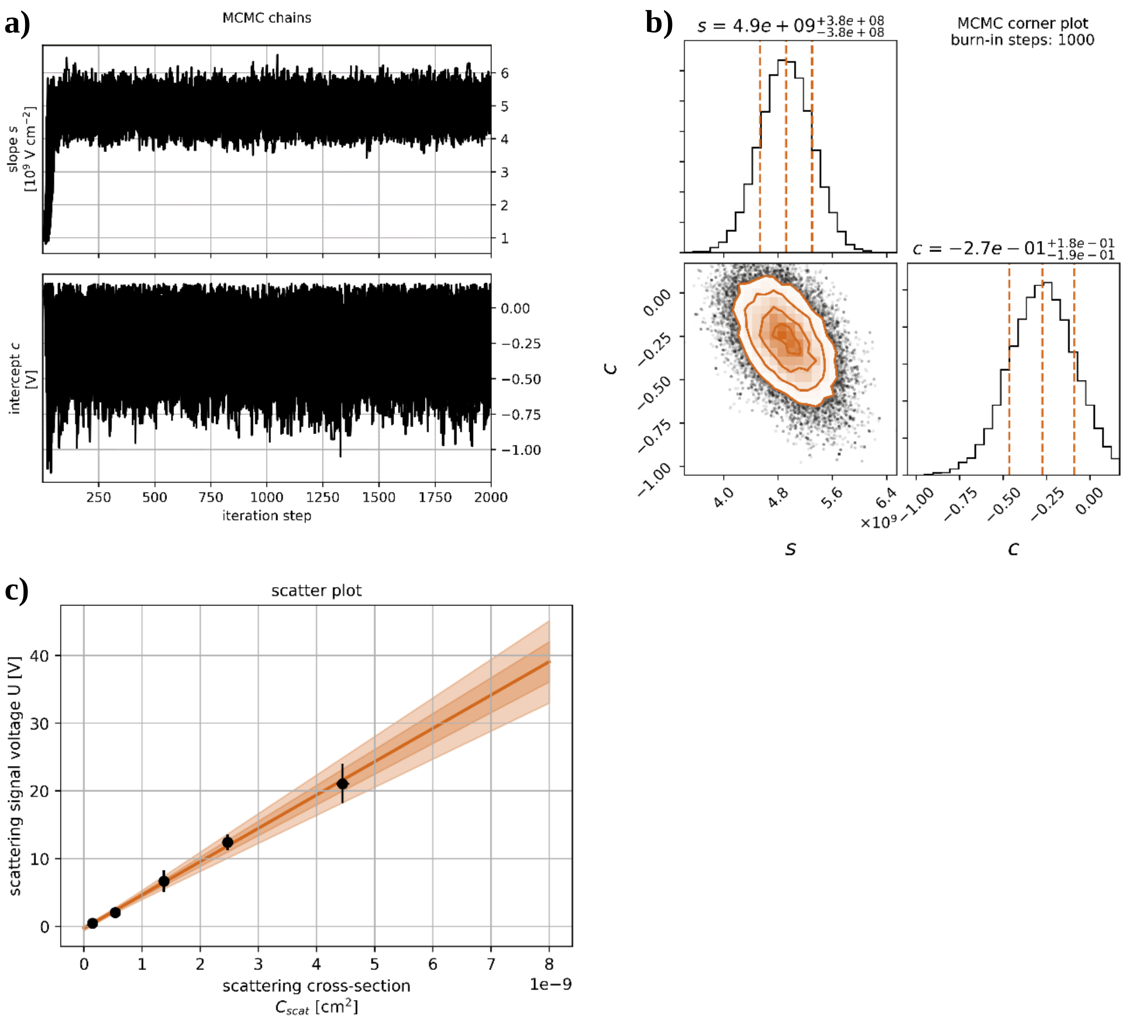

Figure B.1: The figures show the calibration of the OPC1. In **(a)** the calculation of slope s and intercept c of the MCMC (Markov chain Monte Carlo) method is represented. Overall 2000 iteration steps were considered in this calculation. Panel **(b)** shows the probability density function of the instrument parameters, including median and the 16th and 84th percentile. The graph in panel **(c)** uses these values for the representation of the linear correlation between the scattering cross section and the scattering signal voltage. The black dots are the measurement of the PSL particles and the red brown line gives the best fit of the linear function. The shaded area shows the range between the 16th and 84th percentile.

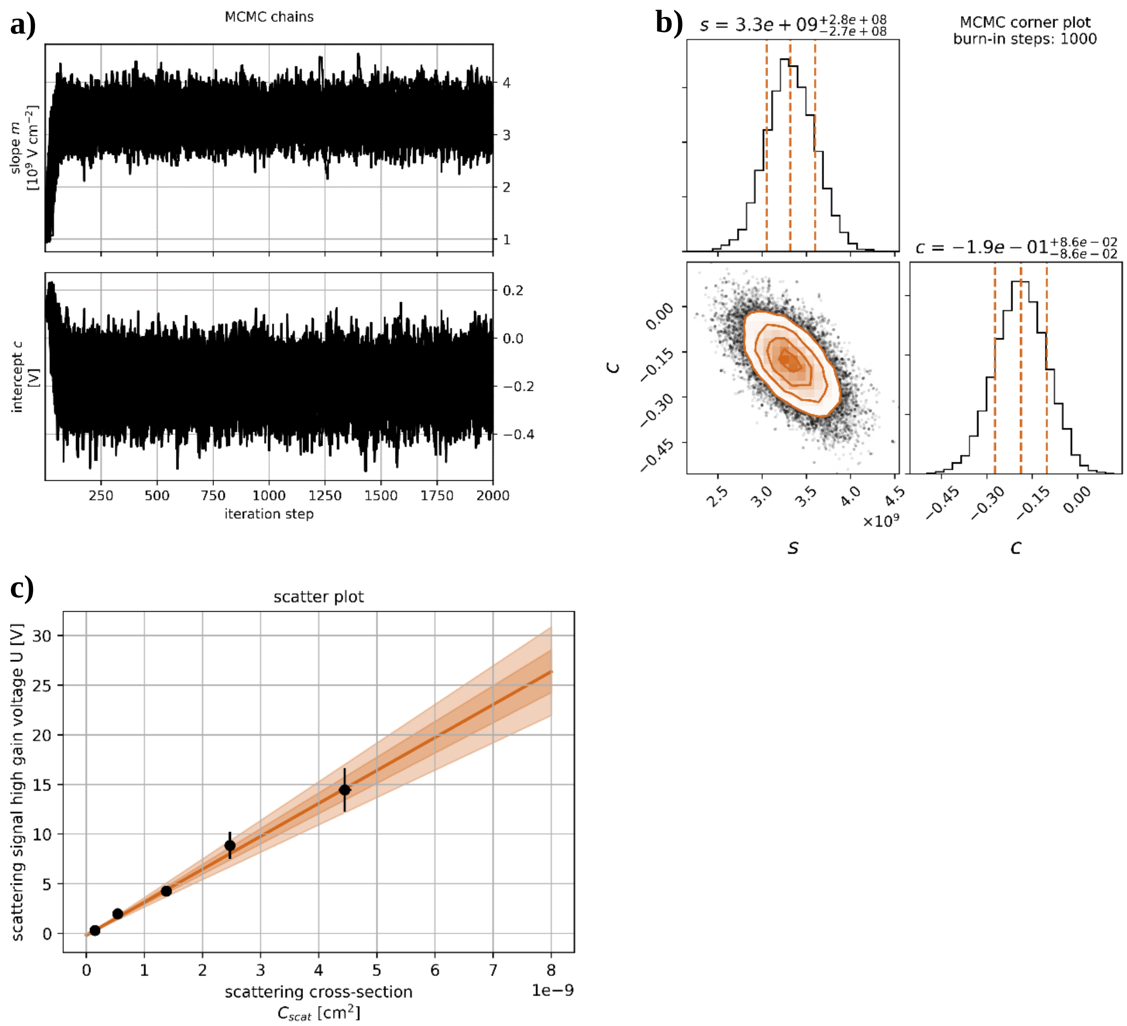

Figure B.2: The parameter solution ensemble presented in the same way as in B.1, calculated for OPC2.

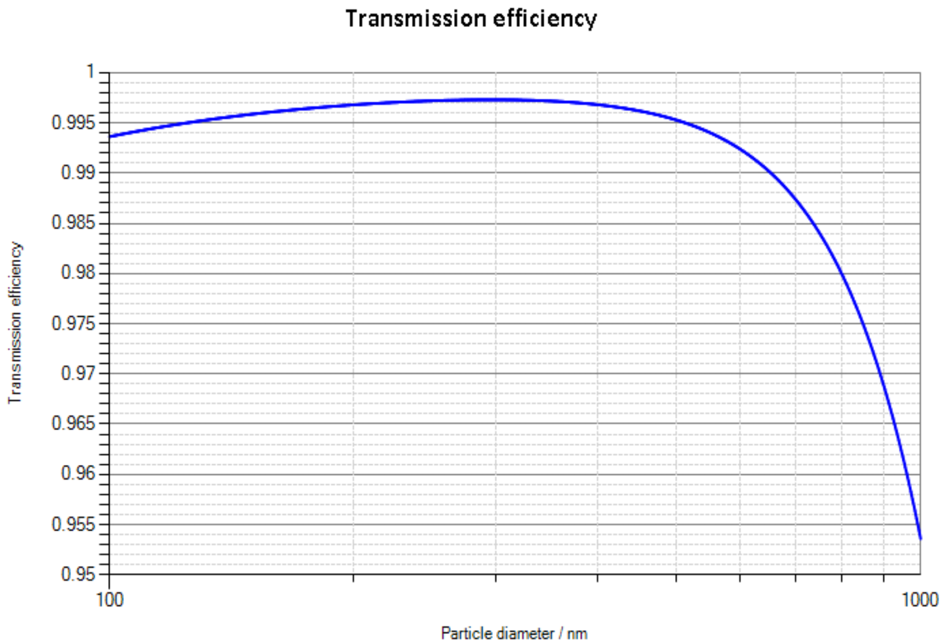

Figure B.3: The transmission efficiency of the Thermodenuder for a diameters range from 100 to 1000 nm calculated with the PLC (von der Weiden et al., 2009).

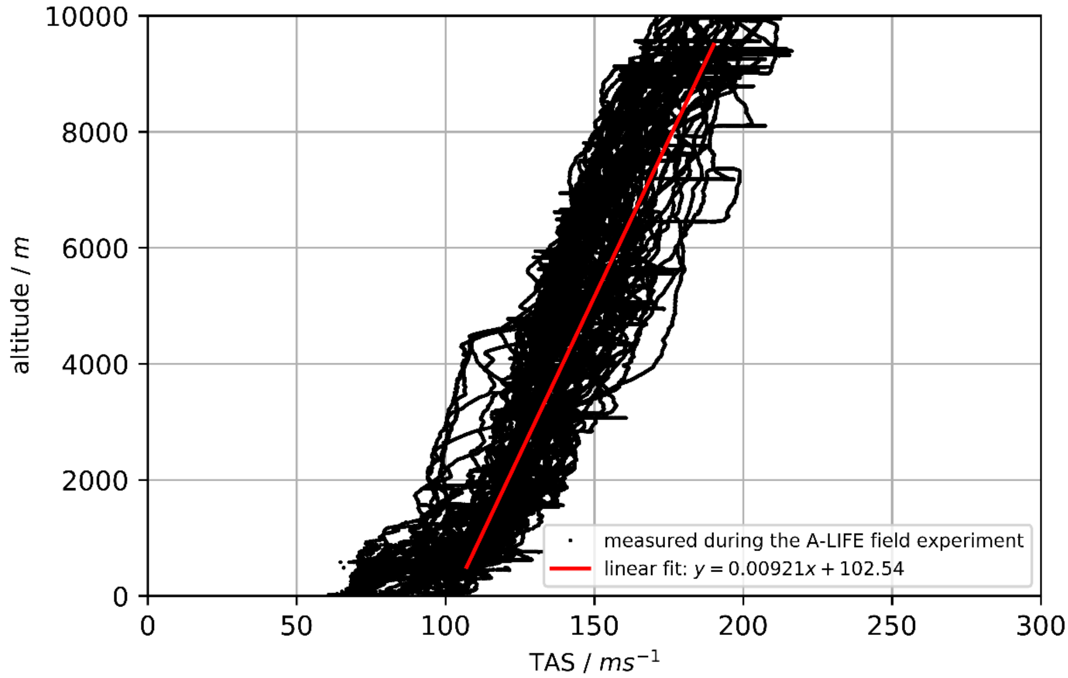

Figure B.4: The measured TAS of the Falcon during the whole A-LIFE field experiment are shown with black dots. The red line represents the linear fit calculated for an altitude range of 500 m up to 9500 m used for the cutoff-diameter calculation in Fig. 4.1.1 and 4.2.1.

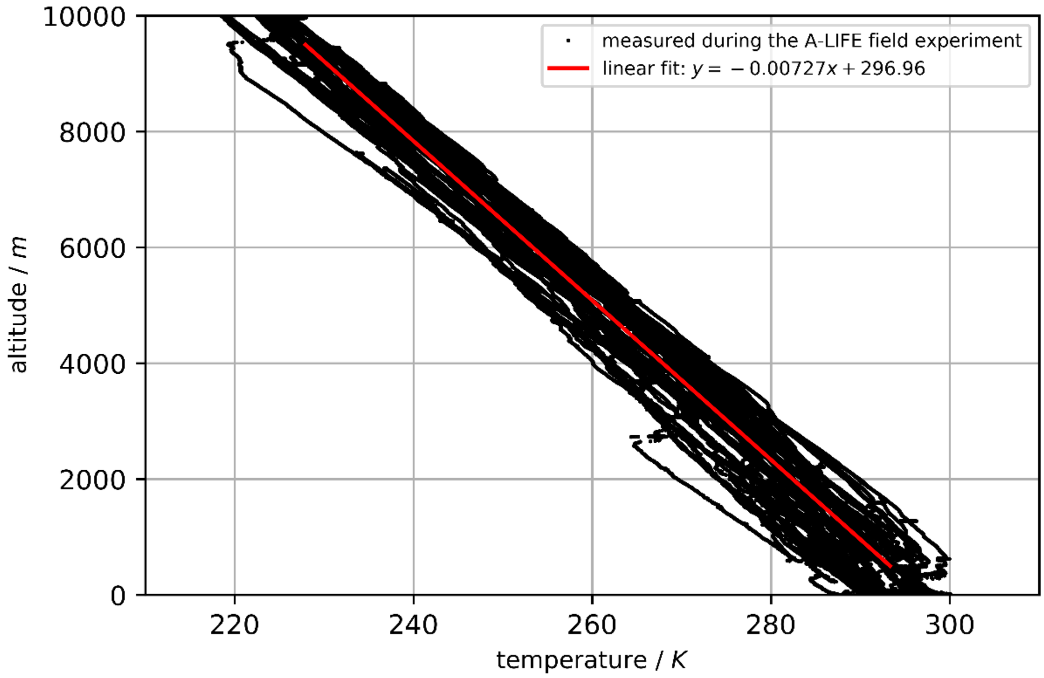

Figure B.5: The measured ambient temperatures during the whole A-LIFE field experiment are shown with black dots. The red line represents the linear fit calculated for an altitude range of 500 m up to 9500 m used for the cutoff-diameter calculation in Fig. 4.1.1 and 4.2.1.

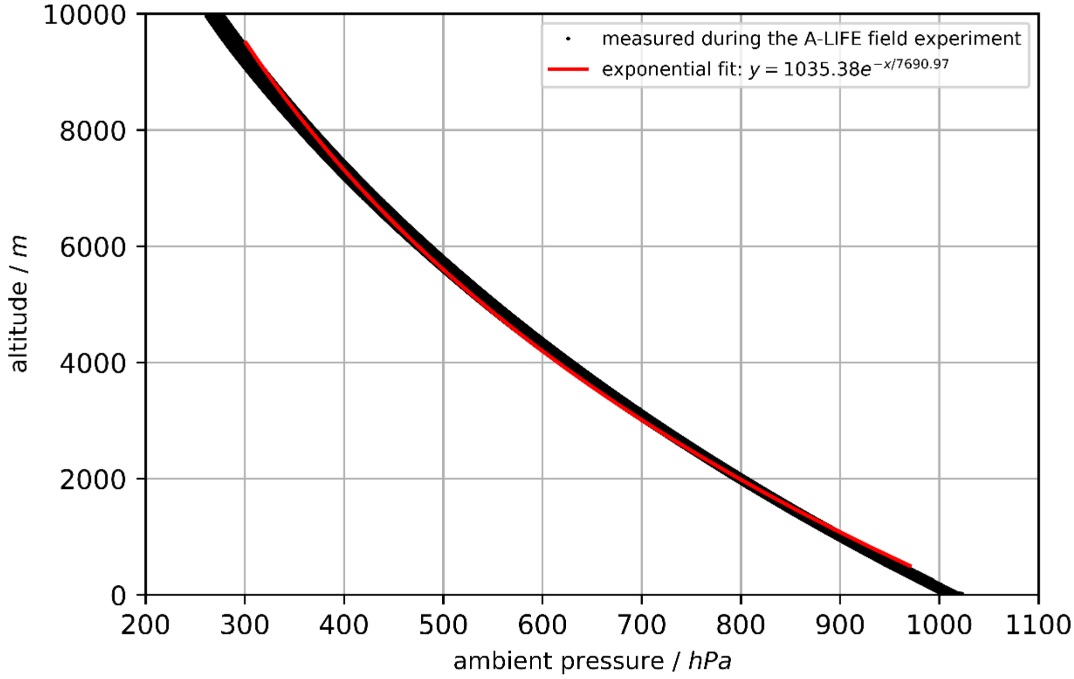

Figure B.6: The measured ambient pressures during the whole A-LIFE field experiment are shown with black dots. The red line represents the exponential fit calculated for an altitude range of 500 m up to 9500 m used for the cutoff-diameter calculation in Fig. 4.1.1 and 4.2.1.

Bibliography

Baumgardner, D., H. Jonsson, W. Dawson, D. O'Connor, and R. Newton. 2001. "The Cloud, Aerosol and Precipitation Spectrometer: A New Instrument for Cloud Investigations." *Atmospheric Research* 59: 251–64. https://doi.org/10.1016/S0169-8095(01)00119-3.

Boucher, O., D. Randall, P. Artaxo, C. Bretherton, G. Feingold, P. Forster, V.-M. Kerminen, et al. 2013. "Clouds and Aerosols. In: Climate Change 2013: The Physical Science Basis. Contribution of Working Group I to the Fifth Assessment Report of the Intergovernmental Panel on Climate Change [Stocker, T.F., D. Qin, G.-K. Plattner, M. Tignor, S.K. Allen, J. Bos." Cambridge, United Kingdom and New York, NY, USA. https://doi.org/10.1017/CBO9781107415324.016.

Dogan, G., G. Güllü, and G. Tuncel. 2008. "Sources and Source Regions Effecting the Aerosol Composition of the Eastern Mediterranean." *Microchemical Journal* 88 (2): 142–149.

Dollner, Maximilian. 2015. "Vertical Distribution of CCN Properties in the Caribbean during SALTRACE." Master thesis. Ludwig-Maximilians-Universität München.

Fiebig, Markus. 2001. "Das Troposphärische Aerosol in Mittleren Breiten - Mikrophysik, Optik Und Klimaantrieb Am Beispiel Der Feldstudie LACE 98." PhD-thesis. Ludwig-Maximilians-Universität München.

Grimm. 2010. *Grimm SkyOPC 1.129 User Manual*. 2.4.

Hinds, William C. 1999. *Aerosol Technology: Properties, Behavior, and Measurement of Airborne Particles*. John Wiley & Sons.

Kaaden, N., A. Massling, A. Schladitz, T. Müller, K. Kandler, L. Schütz, B. Weinzierl, A. Petzold, M. Tesche, S. Leinert, C. Deutscher, M. Ebert, S. Weinbruch and A. Wiedensohler. 2009. "State of Mixing, Shape Factor, Number Size Distribution, and Hygroscopic Growth of the Saharan Anthropogenic and Mineral Dust Aerosol at Tinfou, Morocco." *Tellus B* 61: 51–63. https://doi.org/10.1111/j.1600-0889.2008.00388.x.

Kulkarni, P., Baron, P. A., Willeke, K. 2011. *Aerosol Measurement: Principles, Techniques, and Applications*. 3rd ed. John Wiley & Sons.

Lance, S., A. Nenes, J. Medina, and J. N. Smith. 2006. "Mapping the Operation of the DMT Continuous Flow CCN Counter." *Aerosol Science and Technology*, 242–54. https://doi.org/10. 1080/02786820500543290.

Myhre, G., D. Shindell, F.-M. Breon, W. Collins, J. Fuglestvedt, J. Huang, D. Koch, et al. 2013. "Anthropogenic and Natural Radiative Forcing. In: Climate Change 2013: The Physical Science Basis. Contribution of Working Group I to the Fifth Assessment Report of the Intergovernmental Panel on Climate Change [Stocker, T.F., D. Qin, G.-K. Plattner, M. Ti." Cambridge, United Kingdom and New York, NY, USA. https://doi.org/10.1017/ CBO9781107415324.018.

Roberts, G. C., and A. Nenes. 2005. "A Continuous-Flow Streamwise Thermal-Gradient CCN Chamber for Atmospheric Measurements." *Aerosol Science and Technology* 39: 206–21.

Rosenberg, P D, A R Dean, P I Williams, J R Dorsey, A Minikin, M A Pickering, and A Petzold. 2012. “Particle Sizing Calibration with Refractive Index Correction for Light Scattering Optical Particle Counters and Impacts upon PCASP and CDP Data Collected during the Fennec Campaign.” *Atmos. Meas. Tech.* 5: 1147–63. https://doi.org/10.5194/amt-5-1147-2012.

Seinfeld, J., and S. Pandis. 2006. *Atmospheric Chemistry and Physics: From Air Pollution to Climate Change*. 2nd editio. John Wiley & Sons.

Szymanski, W. W., and B. Y. H. Liu. 1986. “On the Sizing Accuracy of Laser Optical Particle Counters.” *Particle & Particle Systems Characterization* 3: 1–7. https://doi.org/10.1002/ppsc.19860030102.

Walser, Adrian. 2017. “On the Saharan Air Layer Aerosol and Its Role as a Reservoir of Cloud Condensation Nuclei.” PhD-thesis. Ludwig–Maximilians–Universität München.

Walser, Adrian, Daniel Sauer, Antonio Spanu, Josef Gasteiger, and Bernadett Weinzierl. 2017. “On the Parametrization of Optical Particle Counter Response Including Instrument-Induced Broadening of Size Spectra and a Self-Consistent Evaluation of Calibration Measurements.” *Atmospheric Measurement Techniques* 10 (11): 4341–61. https://doi.org/10.5194/amt-10-4341-2017.

Weiden, S.-L. von der, F. Drewnick, and S. Borrmann. 2009. “Particle Loss Calculator – a New Software Tool for the Assessment of the Performance of Aerosol Inlet Systems.” *Atmos. Meas. Tech.* 2: 479–94. https://doi.org/10.5194/amt-2-479-2009.

Weinzierl, Bernadett. 2008. “Radiatively-Driven Processes in Forest Fire and Desert Dust Plumes.” PhD-thesis. Ludwig-Maximilians-Universität München.

Wendisch, M., and J.-L. Brenguier. 2013. *Airborne Measurements for Environmental Research: Methods and Instruments*. John Wiley & Sons.

Acknowledgments

An dieser Stelle möchte ich mich ausdrücklich bei den Menschen bedanken, die mich während der Anfertigung dieser Masterarbeit unterstützt und motiviert haben und ohne denen der Abschluss meines Studiums nicht möglich gewesen wäre.

Zuerst gebührt mein Dank Bernadett Weinzierl, die meine Masterarbeit betreut und begutachtet hat. Für die hilfreichen Anregungen und die konstruktive Kritik bei der Erstellung dieser Arbeit möchte ich mich herzlich bedanken. Des Weiteren möchte ich ihr für das Ermöglichen, in dem tollen Arbeitsumfeld mitwirken zu können, meinen Dank aussprechen. Ich freue mich auf alle kommenden Aufgaben und Herausforderungen, die gemeinsam angepackt werden können.

Ein besonderer Dank gilt auch Adrian Walser, der viel Zeit und Mühe in das Gegenlesen der Manuskripte dieser Arbeit investierte. Aufgrund seiner Kommentare und Anmerkungen konnte die Qualität der Arbeit und meine Kenntnisse der Aerosolphysik deutlich verbessert werden. Außerdem möchte ich ihm herzlich danken für das geduldige und genaue Beantworten meiner vielen Fragen während des Schreibprozesses.

Bedanken möchte ich mich außerdem bei meinen Kollegen der Aerosolgruppe Maximilian Dollner, Josef Gasteiger, Agnieszka Kupc, Katharina Heimerl, Marilena Teri, Clemens Weselka, Antonio Spanu, Judith Kasper und Nikolaus Fölker für die konstruktive Zusammenarbeit und die vielen hilfreichen Tipps und Hinweise.

Des Weiteren bedanke ich mich bei meinem Freund Thomas, der die Arbeit gegengelesen hat und mir nützliches Feedback bezüglich englischer Sprache und Verständlichkeit geben konnte.

Zu guter Letzt möchte ich mich bei meinen Eltern bedanken, die mich über all die Jahre des Studiums hinweg unterstützten und bei meiner Freundin Michaela, die mir vor allem während dem Erstellen dieser Arbeit und in den finalen Semestern des Studiums eine große Hilfe war und mich durch diese Zeit getragen hat.

A-LIFE is an ERC project at the University of Vienna with PI Bernadett Weinzierl. This project has received funding from the European Research Council (ERC) under the European Union’s Horizon 2020 research and innovation program under grant agreement No. 640458. In addition, the German Aerospace Center (DLR) provided funding for a significant amount of flight hours and aircraft allocation days for the A-LIFE aircraft field experiment. Furthermore, two EUFAR projects were clustered with A-LIFE and provided funding for 16 flight hours. Moreover, various groups participated in the A-LIFE field experiment on their own funding.